3-2021

Charge Mitigation Technologies for Aircraft Platforms

Mitchell L. Rudy

Charge Mitigation Technologies for Aircraft Platforms

THESIS

Mitchell L. Rudy, 1st Lt, USAF

AFIT-ENG-MS-21-M-078

DEPARTMENT OF THE AIR FORCE
AIR UNIVERSITY

AIR FORCE INSTITUTE OF TECHNOLOGY

Wright-Patterson Air Force Base, Ohio

AFIT-ENG-MS-21-M-078

CHARGE MITIGATION TECHNOLOGIES FOR AIRCRAFT PLATFORMS

THESIS

Presented to the Faculty

Department of Electrical and Computer Engineering

Graduate School of Engineering and Management

Air Force Institute of Technology

Air University

Air Education and Training Command

in Partial Fulfillment of the Requirements for the

Degree of Master of Science in Electrical Engineering

Mitchell L. Rudy, B.S.

1st Lt, USAF

25 March 2021

AFIT-ENG-MS-21-M-078

CHARGE MITIGATION TECHNOLOGIES FOR AIRCRAFT PLATFORMS

THESIS

Mitchell L. Rudy, B.S.
1st Lt, USAF

Committee Membership:

Andrew S. Keys, Ph.D.
Chair

Stephen C. Cain, Ph.D.
Member

Mark H. Fernelius, Ph.D.
Member

Abstract

Research into ion-based advanced propulsion systems, such as air-breathing Hall effect thrusters on high-velocity aircraft and ion-propelled thrusters on spacecraft, necessitates addressing accompanying residual electric charge accumulation on the ungrounded flight platform. An experimental testbed was constructed to assess charge mitigation technologies and their effectiveness on aircraft. Electrostatic charge was produced by a Van de Graaff generator capable of providing potential differences exceeding a megavolt when combined with a high voltage direct current source generator. This research did not utilize such a source generator and therefore did not reach those potential differences. This research attached an isolated airfoil structure to the Van de Graaff generator's lower terminal to measure induced leakage currents under various applied environmental conditions, including up to three static wicks along the structure's trailing edge, airflow across the structure of up to 10 m/s, and an insulative painted coating. The airfoil was a symmetric teardrop shape; air flowed over the rounded edge first to the tapered edge. Statistical tests indicated airflow improved a conductive airfoil's leakage current at $\alpha = 0.0739$. The average increase was -0.1256 μA. No statistically significant improvements were observed with an insulative airfoil.

Acknowledgements

Studying at AFIT has been a challenging experience. However, the faculty and other students have made it very rewarding. I would first like to thank my advisor, Dr. Andrew Keys, for his mentorship and assistance throughout this entire process. Additionally, I would like to offer a special thanks to Dr. Brian Sell for his extensive support in constructing the test bed (and making sure I was not electrocuted). Last, but certainly most deserving, I would like to thank my wife for staying up with me during the long, school-filled nights and weekends. It helped.

Mitchell L. Rudy

Table of Contents

Page

List of Figures

List of Tables

CHARGE MITIGATION TECHNOLOGIES FOR AIRCRAFT PLATFORMS

I. Introduction

1.1 Background

Current research into advanced propulsion systems such as air-breathing Hall effect thrusters on high-velocity aircraft and ion-propelled thrusters on spacecraft result in the need to address electric charge accumulation within the ungrounded flight platform. Left unchecked, large amounts of electrostatic charge can accumulate on nearby material surfaces and quickly cause undesirable problems. Systems that remain on the Earth's surface can effectively handle the charge and charge carriers by installing a common ground terminal connected between the earth and the charge-generating components. However, if the system is part of an isolated platform, such as an aircraft, spacecraft, or a launch vehicle, a common ground terminal is not an option. This necessitates developing alternative charge mitigation techniques. Handling built-up electric charge on airplanes is not a new concept and has been investigated since the 1940s; corona discharge-based systems have remained the typical solution for low-level charge accumulation. With the development of new technologies for other areas of research, one example being thermionic hollow cathodes for spacecraft propulsion, it is prudent to take inventory and assess whether corona discharge-based systems should remain a first consideration.

1.2 Research Goals and Contributions

This research identifies and reports on technology capable of removing or utilizing electric charge accumulated on an aircraft. An electrostatic testbed was constructed with a one megavolt-capable Van de Graaff generator (VdG) and aluminum airfoil as the centerpieces. Through use of this testbed, the research may assess the effectiveness and practicality of each technology and how airflow enhances their performance if at all. This research focuses on passive copper wicks to establish a baseline that more advanced systems may be compared to.

1.3 Assumptions and Limitations

The research assumed no plasma sheath was present. The research was limited to: a single body to build charge on, a charging current limited to the VdG's output, and airflow velocities were limited to approximately 10 m/s.

1.4 Thesis Organization

This thesis has five chapters. Chapter II discusses the historical motivation for using static wicks on aircraft, electrical discharges with a focus on corona discharges, active corona discharge systems on aircraft, and some alternative electrical discharge applications. Afterwards, it discusses band theory and its relation to electron emission. Next, thermionic emission is discussed, with considerations given to thermionic hollow cathodes and electron guns. The last topics are tribology and VdGs to explain the testbed's charge generation method. Chapter III details the electrostatic testbed's construction and the experiments performed on a small-scale and full-size VdG. Chapter IV presents and analyzes the results from testing the full-size VdG. Finally, Chapter V summarizes the research and identifies future research avenues.

II. Literature Review

2.1 Overview

This chapter covers potential technologies to remove electric charge from an ungrounded platform. It begins with the historical context which motivated the development of static wicks for aircraft. Following that, the chapter discusses different charge emission mechanisms, such as electrical discharges and thermionic emission, and how they are utilized. Finally, it discusses Van de Graaff generators and tribology to develop an understanding of the research's charge generation method.

2.2 History of Aircraft Charge Emission

When aircraft fly through the atmosphere, multiple phenomena may cause electric charge build-up on the body of the airframe. Precipitation static may occur when the aircraft flies through precipitation particulates such as ice, snow, rain or dust. Triboelectric charging [1] may occur as charged particles within the atmosphere quickly contact and move across the aircraft's external surfaces. Additionally, nearby thunderstorm clouds produce electric fields capable of driving currents across the aircraft's surface and unequally building charge on the aircraft's outer body [2]. The charge cannot accumulate indefinitely.

As the aircraft's electric potential rises relative to the surrounding air, corona areas develop at extremity locations such as antennas and wing tips [3]. The large number of ions at these locations may result in rapid corona discharges [3]. These discharges cause a significant amount of undesirable electromagnetic noise which adversely affects communication and navigation equipment operation [3]. The magnitude of this interference is dependent upon the source charge's strength, any coupling between the discharge source and the antennas, as well as the discharge current [1]. The most

common solution for this problem was static wicks [4], which are still the standard method for dissipating charge on most aircraft [5] experiencing low levels of charge accumulation.

The precipitation static problem started appearing as more aircraft were outfitted with radio communications in the 1920s; its seriousness was brought front and center by aircraft and human losses at the start of World War II [3], [6]. To combat the problem, a joint committee involving the United States Army and Navy was assembled in 1943 [3]. The committee investigated several types of dischargers and reported textile wicks, modified to be slightly conductive, with frayed ends were an ideal option and should be combined with other measures such as dielectric coatings on antennas [3]. Although the wicks were slightly conductive, the discharge locations were connected to the aircraft through a highly resistive path [4]. Similar to a passive resistor-capacitor low pass filter, this setup electrically connected the wick to the aircraft while attenuating the Radio Frequency (RF) components. Further, the frayed ends provided sharp points with small radii of curvature and therefore could more easily produce stronger electric fields capable of ionizing the surrounding air.

Decreasing the discharge magnitude helps with RF noise but carries a trade-off of less charge leaving the aircraft. To preserve the amount of removed charge, the discharge frequency could be increased, still at an overall lower noise power, by applying a voltage to the discharging electrode [7]. Forcing the discharge to occur at locations where the aircraft's design provides natural shielding can further help decouple the corona noise [7]. Two suitable places for the discharging elements are the base of a wing or the aircraft's tail [7], [8]. These spots expose the discharger to the surrounding airflow which can carry ions away from the airplane and reduce the space charge around the discharging wick [7]. Handling of RF noise is important in charge mitigation but further discussion is outside the scope of the current research.

2.3 Electrical Discharges

When static wicks are used to remove charge from an aircraft, they do so via corona discharges. Corona discharges occur when the electric field at a point on a conductor, referred to as a discharging electrode, exceeds the dielectric strength of the surrounding gas. As a point of reference, air at 25°C, 76 cmHg (sea level) requires an electric field strength of approximately 30 kV/cm [9], although it can vary based on the electrode's particular geometry. Once the electric field exceeds that critical strength, it can ionize the neutral molecules surrounding the discharging electrode, produce electron avalanches and trigger a discharge. Positive and negative corona have significantly different mechanisms but follow similar trends with increasing discharging electrode voltages [10].

As the electrode's voltage rises, the discharges are initially irregular pulses or bursts but eventually the gas's ionization becomes self-sustained. Raising the voltage from this point results in the system entering a glow discharge regime. Further increasing the voltage leads to streamers and then ultimately ionizes a path between the discharging electrode and another electrode to produce an arc. Observing the intermediary stages depends on having sufficient distance between the two electrodes; too short of a distance results in the system skipping over the intermediary stages straight to arcing. For aircraft applications, the discharges occur in air at varying altitudes which affects the air's dielectric strength.

2.3.1 Electric Breakdown of Air

Air is typically a strong insulator and high voltages are required to produce a strong enough electric field to trigger breakdowns and corona discharges. At sea level, the requisite field strength is about 30 kV/cm. More generally, the electric field strength required for a corona discharge from a wire or cylinder is approximately

given by Peek's law:

$$E = E_0 \delta \left(1 + \frac{c}{\sqrt{\delta R}}\right) \tag{1}$$

where E is the threshold electric field strength required, E_0 is a constant field strength, δ is the relative density of the current atmosphere compared to standard temperature and pressure, c is a constant distance (approximately 0.301 $\text{cm}^{1/2}$ for air), and R is the wire's radius [9]. Although Equation 1 was originally derived empirically, it was derived in [11] from the Townsend gas breakdown criterion:

$$\int \alpha' dr = \ln\left(1/\gamma\right) \tag{2}$$

where α' is the "net ionization coefficient," the difference between the ionization and attachment coefficients, r is a radial distance away from the wire, and γ is the secondary electron emission coefficient.

After plotting α'/N against E/N, where N was the gas density, for past experiments' results, $\alpha^{'}/N$ for wires and cylinders showed a quadratic dependence on E/N up to about 500 Td [11]. Using the quadratic function in combination with an electric field solution from Laplace's equation as the integrand in Equation 2 produced a solution with the form of Equation 1. However, for discharging points, such as the tip of pointed electrode, a linear dependence fit better and extended the applicable domain up to approximately 3000 Td [11]. Solving Laplace's equation again for the electric field and using it with the linear fit as an integrand in Equation 2 produced a similar solution but with an additional $(\delta R)^{-1}$ term [11]. After substituting in constant values appropriate for the experimental trends, the derived expression for the threshold field strength in air was:

$$E = 25\delta\left(1 + \frac{0.35}{\sqrt{\delta R}} + \frac{0.03}{\delta R}\right) \tag{3}$$

In this equation, the field strength is in kV/cm and the discharging point's radius R is in cm. Upon reaching the threshold field strength, discharges can occur.

2.3.2 Trichel Pulses

Trichel pulses, named after G. W. Trichel, are negative corona discharges that continue for a short time (on the order of μs) until the local space charge produces a strong enough electric field to inhibit further discharge [12]. The pulses are characterized by a sharp rise and then drop in discharge current. The voltage threshold V_0 for the pulses to start occurring was found to be independent of cathode material [11],[12] as well as the cathode's tip's radius [13]. Increasing the voltage V applied to the cathode will increase the pulse frequency and time-averaged current as a function of $V(V - V_0)$ [13]. Meanwhile, increasing the cathode's tip radius was found to increase the pulse's period and the amount of charge transferred per pulse [13]. The model frequently used to explain Trichel pulses in electronegative gases is Morrow's model incorporating a plasma of positive and negative space charge as well as secondary electron emission [14].

In Morrow's model, the discharge is initially powered by electron avalanches. However, eventually the cathode's electric field creates a nearby region of positive ions, which increase the discharge current, and a region of electrons farther out. As the discharge continues, the two space charges develop further and, with the help of photoemission, the discharge current peaks. Eventually, the space charge regions form a quasi-neutral plasma which has no electric field at is center. This results in conditions no longer suitable for a self-sustaining discharge and so the discharge current declines. The electrons then tend to bond with nearby air molecules and produce

negative ions. These negative ions as well as the positive ions closer to the discharging cathode have low mobility and halt the discharges. Eventually, the positive ions migrate towards and collide with the cathode and produce electrons which can trigger avalanches and initiate more Trichel pulses. The successive pulses are expected to have smaller amplitudes than the initial pulse due to the preexisting space charge. Recent work has shown that Trichel pulses can occur in non-electronegative gases too and suggests that, while the negative ions do increase the discharge current's decay rate, the positive ions are more important to the overall process [15].

It was mentioned earlier that increasing the voltage applied to the cathode's tip increases the repetition frequency of the Trichel pulses. However, the frequency cannot increase indefinitely. The particular limit depends upon electrode dimensions and surface properties, but tends to be higher for more pointed electrodes and higher for smaller electrodes [16]. Raising the applied voltage after the pulses reach that critical frequency transitions the discharge into a pulseless glow discharge [16].

2.3.3 Glow Discharge

A glow discharge follows after Trichel pulses, but mostly happens when using oval or spherical electrodes [17]. Creating a steady glow discharge with the typical needle-to-plane setup is difficult because the space charge density drops when moving away from the cathode and results in a weaker electric field [18]. Supplying additional voltage to the cathode does increase the current supplied to the space charge regions but doing so can easily result in a spark instead [18]. To stabilize the glow discharge, techniques such as flowing air over the cathodes can be implemented [19]. Doing so supports developing a stable glow discharge by controlling ionization instabilities which in turn allows significantly higher discharge currents [19]. Raising the cathode's voltage further will create a negative streamer discharge, provided there

is a sufficiently large gap. The streamers will begin occurring when the electron avalanches create enough additional electrons to form a space charge that produces an electric field strength equivalent to the breakdown field strength [16].

2.3.4 Charge Control Systems

2.3.4.1 Cornell's System and Discharge Current Relationships

An "active corona discharge system" was developed by Cornell Aeronautical Laboratory in the early 1950s and operated with the intent to remove all electrostatic charge from a flying aircraft [8]. The system featured two electric field meters whose readings controlled a 100 kV dc voltage supply [8]. The fields measured by the sensors were combinations of ambient electric fields and electric fields generated by static charge. The supply had one terminal connected to the aircraft's surface and the other to an insulated corona point 40 cm behind the airplane's tail [8]. Chapman characterized Cornell's system's performance via a "blow-away current" describing the current blown away from the aircraft after a discharge [8].

The testing setup used by Chapman featured up to five discharging points arranged on a 9.525 cm diagonal square with a plate 11.43 to 19.05 cm away from the tips of the points [8]. When using a separation distance of 19.05 cm, the single point produced a current of 130 μA while five points produced a current of 225 μA [8]. The five-point setup did not produce five times the discharge current because the space charge from each discharge dampened the effectiveness of the other dischargers.

The region immediately around a discharge point can be modeled as a sphere of space charge where electrostatic forces dominate over the wind forces [8]. In the presence of wind, a cylinder of space charge, oriented in the direction of air flow, stretches out from the sphere and charge is carried through the cylinder by the wind [20]. Analysis by Chapman showed modeling the cylinder as a truncated paraboloid

did not change the fundamental relationship and only modified the values of constant coefficients by a few percent [8]. A truncated paraboloid could be used to model the space charges' spread due to the repulsive coulomb force. Reconciling these two space charge distributions results in expressions for the corona discharge current.

The mathematical relationships driving the corona discharge current vary with respect to the voltage applied to the discharging electrode and the wind speed. When an electric potential is applied to the electrode and there is no wind, the discharge current, I, is proportional to the square of the applied voltage, V, and ion mobility, μ: $I \propto \mu V^2$ [21]. On the other hand, flowing air at speed w over the discharge point while applying a potential adds a term that is proportional to the product of the applied voltage and the wind speed: $I \propto wV$ [8], [20], [21]. The linear voltage relationship was tested for air speeds up to 400 m/s [21]. Between these two terms, the squared voltage dominates at lower air speeds and the voltage-wind speed product dominates at higher air speeds [21]. These expressions do assume that the applied voltage is much greater than the corona discharge starting voltage, V_0; when V does not significantly exceed V_0, one instance of V is replaced by $V - V_0$ in each expression [20]. If no voltage is applied to the electrode, the current is expected to be proportional to the wind speed squared on the basis of dimensional analysis; wind tunnel tests reportedly showed the current varying with the wind speed raised to a power [8]. The analysis on a single discharge point could be extended to multiple points provided the electrostatic-dominated regions did not overlap [8].

2.3.4.2 Helicopters

Helicopter discharging was investigated in the early 1960s with the goal of keeping the aircraft's electrostatic energy level below 1 mJ with respect to earth [22]–[24]. Electrostatic energy with respect to earth was considered because an aircraft can

undergo corona discharges and have its electric potential match the surrounding air but still possess electrostatic energy [22]. Leaving the charge unaccounted for carried the risk of shocking personnel or igniting flammable and explosive substances [22]. The work of [22] casted the problem as a charging and discharging resistor-capacitor circuit and so any discharging system should reduce the surrounding air's resistivity. Doing so would decrease the discharging time constant and prevent the system from reaching a voltage significantly different from the surrounding air [22]. Using an active corona discharge system was evaluated as the best option.

The electrostatic discharger system discussed in [23] utilized both positive and negative active corona discharge points connected to high-voltage DC power supplies. The system assessed the aircraft's potential with respect to the surrounding air with a passive discharge point connected to the helicopter via resistive elements [23]. The helicopter's polarity would draw a discharge current across the resistive components, create a positive or negative voltage drop, and then provoke a control signal for the power supplies. The power supplies were configured so one had its positive terminal connected to the positive discharge point and its negative terminal connected to a common ground, while the other had its positive terminal connected to the same ground and its negative terminal connected to the negative discharge point [23]. The discharge points were placed on the ends of opposite rotor blades to utilize the air speed while also accelerating charge carriers radially away from the helicopter [23]. The current discharged from a single corona point with 20 kV applied and air speeds exceeding 152.4 m/s was approximately 40 μA [23]. Flight tests with the system on an H-37 showed that it achieved the electrostatic energy goals [23].

The system described in [24] also had positive and negative corona discharge points, but instead located them on the helicopter's tail boom for design simplicity. Further, the system tracked the aircraft's potential via an electrostatic field meter

installed on a panel underneath the helicopter [24]. Flight tests with a CH-37 showed that the system could maintain the energy below 1 mJ while being charged at a rate of 50 μA [24].

2.3.4.3 Aircraft

An active electrostatic charge control system was developed for vertical takeoff and landing (VTOL) and jet aircraft in the late 1960s and was described in [25]. An active system was favored over a passive system to better control the aircraft's voltage whether it needed to be closer to ground or at an arbitrary value; the latter situation would arise during refueling operations. The system itself had a single set of non-wick corona discharge points along the entire stationary trailing edges of both wings. The presence of space charge from each point discharging imposed a limit on the current from that point. So, all the points were individually required to reach desirable discharge currents.

To accommodate positive and negative discharges from the same points, two high-voltage power supplies, one for each wing, were developed to provide from -60 kV to 60 kV. The aircraft's electric field was measured to control the supply. The system was tested on a Boeing 707 by manually charging the aircraft to -60 kV and 130 kV, switching the system to automated operation, then measuring the aircraft's steady-state potential. The active discharge system returned the aircraft's potential near zero within one to one-and-a-half seconds, output total discharge currents reaching 800 μA, and adjusted to environmental changes.

2.3.4.4 Lightning Avoidance

Positive corona discharges have been investigated to reduce the chance lightning will strike an aircraft [26], [27]. Aircraft flying through locations with strong ambient

electric fields may become polarized. The resulting surface electric fields may become strong enough to initiate a bidirectional leader from the oppositely charged regions [26]. Positive leaders tend to occur first, due to lower field strength thresholds than negative leaders, and leave the aircraft more negatively charged; this gives rise to negative field strengths capable of initiating negative leaders [26].

Positive corona discharges from both an electrically floating sphere and wing placed in a wind tunnel were able to negatively bias the objects [28]. The discharging electrodes were biased 11 kV above the body and the wind speeds went up to 40 m/s. Their results showed that higher wind speeds resulted in more negative body potentials up to a voltage where higher speeds had no effect. At that voltage, the body's electric field exerted attractive forces on discharged positive ions that the wind could not overcome. For that reason, higher wind speeds resulted in lower corona discharge current. However, when the wing was grounded, the corona discharge current increased with increasing wind speeds [27].

2.3.5 Airflow Control

2.3.5.1 Plasma Actuators

Dielectric barrier discharge (DBD) plasma actuators are devices capable of controlling airflow [29] over different structures and have been investigated in airspeeds reaching supersonic [30], [31] and hypersonic airspeeds [32], [33]. A DBD involves two electrodes, with at least one insulated by a dielectric, separated by a gas and connected to opposite terminals of an AC voltage source [34], [35]. The particular electrode configuration, some possible orientations are shown in Figure 1 below, classifies the DBD as either a volume or a surface discharge. The classification identifies whether the discharge occurs through the separating volume or along the dielectric surface. Prevalent plasma actuator designs create surface discharges.

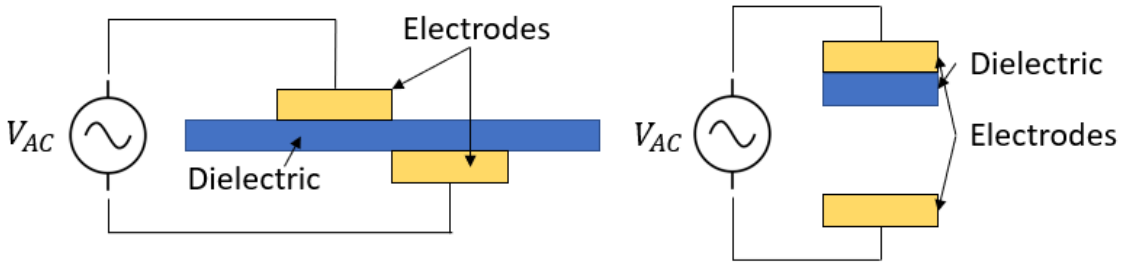

Figure 1. Surface (Left) and Volume (Right) DBD configurations

The single dielectric barrier discharge (SDBD) plasma actuator is a common design and a simplified setup is shown in Figure 2 below where the offset is chordwise [36]–[38]. When the exposed electrode operates as a cathode and has a high enough voltage, it discharges to the insulated electrode. During the discharge, air between the two electrodes ionizes and forms a plasma. Negative charge accumulates on the dielectric layer until the potential difference with respect to the cathode is too small to support the discharge [36]. When the dielectric-insulated electrode operates as the cathode, charge on the dielectric's surface travels to the exposed electrode [36]. The electric field between the two electrodes exerts a force to the plasma's charged particles; these particles collide with the surrounding air, transfer momentum, and thereby modify the airflow. Other actuator designs incorporate corona discharges by introducing an electrode with a DC voltage.

Sliding discharge (SD) plasma actuators retain the electrodes connected to an AC voltage supply while introducing an electrode with a DC voltage [37]. The AC voltage serves to ionize the air while the DC component creates a corona discharge between electrodes [37]. The ionization from the AC voltage stabilizes the corona discharge and, provided the DC voltage is not too great, mitigates arcing potential [39]. The formation of a SD still requires an adequate voltage difference between the DC electrode and whichever other electrode it shares a surface with [40]. Variations

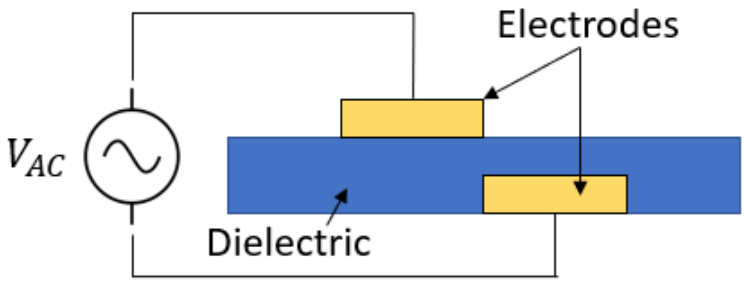

Figure 2. A single DBD (SDBD) configuration fully insulates one of the surface DBD configuration's electrodes. The upper electrode is exposed to airflow

on this actuator exist and some are shown in Figure 3 below. Recent designs such as Zheng's and He's [41], [42] have included a second DC electrode.

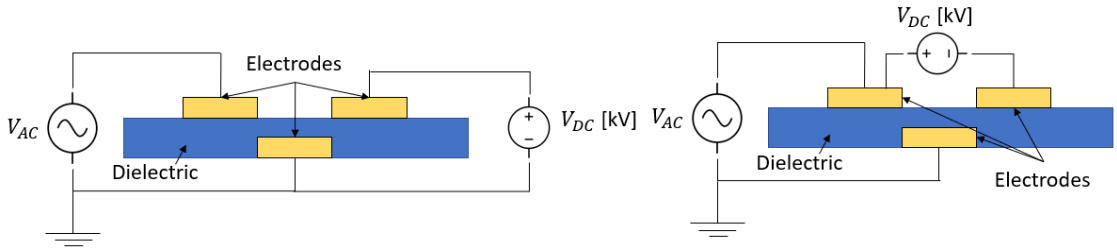

Figure 3. Two possible sliding DBD (SD) configurations. This configuration adds an electrode with a high DC voltage that results in a sliding discharge between the two upper electrodes

The SD actuator tested in [43] induced airflow in almost any direction away from the surface by varying the peak-to-peak AC voltage. The AC and DC electrodes created jets towards the other which collided and produced an upward jet [44]. The DC electrode's jet results from the electrode repulsing ions with the same polarity [44]. The AC electrode's jet arises due to the large voltage difference existing between the AC and DC electrodes creating a strong electric field [44].

2.3.5.2 Propulsion

When charged particles leave a surface during a corona discharge, they are repelled by the material's electric field. As the particles travel, they gain energy and momentum. Eventually, the particles collide with air particulates and transfer their momentum. This generates an airflow called ionic wind. Additionally, from Newton's third law of motion, an equal and opposite force arises which can be used for thrust. Using this thrust to propel an aircraft is the basis of electroaerodynamics (EAD) [45], [46], also called electrohydrodynamics (EHD) when considering air to be a fluid [47], [48]. This manner of propulsion commonly uses a wire-to-cylinder setup [47].

In the wire-to-cylinder setup, there are two parallel cylinders and one is much larger than the other. By comparison, the smaller cylinder appears like a sharp "wire". The smaller cylinder is labeled the emitter electrode while the larger cylinder is the collector electrode. To trigger a corona discharge, a high voltage in the tens of kV is applied across the two electrodes. As a potential gradient develops between the electrodes, the air surrounding the emitter starts to breakdown because it has a strong local electric field. Charge carriers travel between the emitter and collector electrodes and transfer momentum as described in the previous paragraph. Implementing this type of system would make use of excess charge building on an aircraft, but it would not be a good charge mitigation technique because the emitter-collector system creates a closed circuit loop.

2.4 Band Theory

Valence electrons at a material's surface may overcome attraction to nuclei and leave the surface of a material when supplied with enough energy. That energy can come from different sources such as energetic photons or heat. The work function ϕ

identifies the required energy and is material specific. A material's work function is measured as the difference between the Fermi level and the to-be-emitted-to-region's local vacuum level [49]. The Fermi level is an energy state that has a fifty percent chance of being occupied. The local vacuum level is the energy of an electron at rest just outside the material's surface. Not all electrons in a material have the same amount of energy, instead their energies are statistically distributed. Gases or plasmas may have electron energies following a Maxwell-Boltzmann distribution. On the other hand, crystalline solids, which metals typically are, have electrons energies distributed across ranges called bands. Two significant energy bands are the conduction and valence bands.

The conduction band contains electrons that are energetic enough to be conducted into an electric current. Meanwhile, the valence band contains valence electrons which can be elevated into the conduction band by supplying energy to the material. The spacing (or lack thereof) between these two bands, called a band gap, classifies materials as insulators, semiconductors, or metals. Insulators have larger band gaps than semiconductors while metals do not have a band gap. Instead, a metal's valence and conduction bands overlap. For insulators and semiconductors, the Fermi level will lie in the band gap. For metals, however, the Fermi level will lie in the overlapping region. These bands, and others, arise because, as the atomic spacing decreases, the outer electrons of different atoms interact with each other.

The development of energy bands is explained by the Kronig-Penney model [50] which built off the work of Bloch [51]. Bloch's theorem states that, when an electron's potential energy is periodic, then its wave function is periodic over the same region. In the Kronig-Penney model, the electron's potential well is defined in terms of a periodic train of rectangular pulses. Each pulse has a zero-valued portion and a positive portion and an electron wave function assigned to each of those portions.

Imposing boundary conditions on the wave functions and solving the resulting system of equations produces a transcendental equation. The transcendental equation is a function of factors such as the pulses' amplitudes and periodicity. The electron energies which allow the equation to be solved are allowable electron energy states. On the other hand, the electron energies which produce an unsolvable equation are the unallowable states. Together, the sets of allowable and unallowable energy states define the electron energy bands and gaps. Within each band, the possible electron energies are discrete but spaced finely enough to appear continuous.

The likelihood of an electron in a solid having a particular energy level E is given by the Fermi-Dirac (FD) distribution. The distribution function $f_{FD}(E)$ is given by

$$f_{FD}\left(E\right) = \left(1 + \exp\left(\frac{E-\mu}{k_b T}\right)\right)^{-1} \tag{4}$$

where μ is the chemical potential (also called the Fermi level), k_b is the Boltzmann constant, and T is the temperature [52]. As the material's temperature tends towards absolute zero, the Fermi level identifies the highest energy state occupied by an electron. The limiting behavior of $f_{FD}(E)$ as $T \to 0$ is zero when $E > \mu$ and is one when $E < \mu$. Additionally, at absolute zero, the Fermi level is referred to as the Fermi energy and is given by E_F. Materials with a positive E_F may reasonably approximate $\mu \approx E_F$ up to a temperature approximately given $E_F/(\pi k_b) > T$. Above that point, μ may be better approximated by series approximations such as [53]:

$$\mu\left(T\right) = \left(1 - \frac{1}{12}\left(\frac{\pi k_b T}{E_F}\right)^2 - \frac{1}{80}\left(\frac{\pi k_b T}{E_F}\right)^4 - \frac{247}{25920}\left(\frac{\pi k_b T}{E_F}\right)^6\right) E_F \tag{5}$$

By inspection of Equation 4, raising a material's temperature increases the likelihood that an electron is occupying one of the higher-energy states. This sets the stage for thermionic emission.

2.5 Thermionic Emission

Heating a metal and having electrons leave its surface was originally viewed as electrons evaporating off the surface into an electron gas [54]. That analysis produced the well-known Richardson-Laue-Dushman equation:

$$J = AT^2 \exp\left(\frac{-\phi}{k_B T}\right) \tag{6}$$

where J is the current density, A is a constant, T is the temperature, ϕ is the material work function, and k_b is the Boltzmann constant. Originally, the constant A was simply equivalent to

$$A = 4\pi q m k_b^2 / h^3 \tag{7}$$

where q and m are an electron's charge magnitude (C) and mass (kg) and h is Planck's constant (J· s); the product of Equation 7 approximately equals 120.173 A·cm^{-2}· K^{-2} [53]. However, the particular value is material-dependent [55] and affected by electrons in the surrounding gas entering and leaving the emitter [56]. A material's work function is also not always constant and may be affected by its temperature and surface conditions.

Factors such as a material's temperature and surface conditions may affect the work function. Varying a material's temperature can affect thermal expansion as well as an atom's kinetic energy. These in turn can affect a material's work function [57], [58]. Additionally, the emitting surface's electron distribution can create dipoles affecting the work function [49]. Another significant factor is the Schottky effect: an electric field at the emitting location can reduce the potential barrier electrons need to overcome to escape the material surface [53].

2.5.1 Hypersonic Cooling

Thermionic emission, via Electron Transpiration Cooling (ETC), has been proposed to cool the leading edges of hypersonic vehicles [59]–[63]. In ETC, energetic electrons exit from the leading edge, then flow through the air to a point further back on the vehicle and deposit their energy [59]. This technique transfers heat from the hot leading edges, where typical heat control systems would negatively impact the lift-to-drag ratio (L/D), to a region more accommodating of those systems [59]. When the vehicle is negatively biased, more electrons are emitted from the surface and more cooling may occur [63]. Since the electrons travel back to the vehicle and form a closed circuit, this technique does not present much charge control.

2.5.2 Hollow Cathodes

Electric propulsion of spacecraft utilizes combinations of electric and magnetic fields to accelerate and expel plasma from a spacecraft, thereby generating thrust [64]. One way to create the plasma is with thermionic hollow cathodes [65]. An inert gas, such as Xenon, flows out of the device and in the process is ionized by electrons emitted from the heated cathode [66]. One prevalent cathode material is lanthanum hexaboride (LaB6). This material is widely used because it can discharge significant current densities, such as 10 to 20 A/m^2 [67], [68] and can resist impurities in the gas [65]. The ability to resist impurities means that higher partial pressures of substances such as water and oxygen are required to diminish the current emitted by a LaB6 hollow cathode. That being said, LaB6 and other variants are typically tested in vacuum-like conditions and high pressure can mean mTorr. For example, introducing oxygen with a partial pressure of 10^{-2} torr to LaB6 operating at 1570 degrees Celsius can cut off the emitted current [65]. As such, hollow cathode performance metrics are not necessarily extendable to typical aircraft environments.

In addition to working around impurities, the presence of ambient air would reduce the emitted electron's mean free path and necessitate a higher pressure for the propellant. That being said, some designs have considered propelling vessels with ambient air [69], [70] – albeit at low Earth orbit. Micro hollow cathode discharges do exhibit thermionic emission at atmospheric pressure because the cathode's micrometer size allows it to heat quickly [71], [72]. Peak currents of 30 A with a density of 10^5 A/m^2 were reported [72].

2.5.3 Electron Guns

Electron guns are devices that accelerate and focus electrons into a collimated beam via a series of anodes. The devices are constructed to produce the beams in vacuum environments to avoid collisions between air particulates and electrons as well as reactions between emissive materials and air. The electron can originate from sources such as thermionics [73]–[79], field emission [80], plasma discharges [81], [82], and photoemission [83], [84]. Regardless of the electron's source, it will need to migrate from the vacuum to the atmosphere through an electron exit window (EEW).

A Si_3N_4 membrane has been investigated as an EEW [76], [85], [86]. Si_3N_4 has receieved consideration because it can be manufactured with a thickness under a micrometer, and it "has high yield strength (14 Gpa), superior thermal shock resistance (>600 σK), good oxidation resistance, low thermal expansion (3.3×10^{-6}/K) and high temperature range (melting point: 2660K - 2770 K)" [85]. The membrane by itself is not thermally or electrically conductive enough, so a gold film was applied to mitigate charge accumulation and heating [86]. Tests where a tungsten filament produced a 10 μA current in vacuum were able to measure atmosphere ion currents between 2.5 and 4 μA [86]. However, this required a $\pm$10 kV collector electrode positioned one centimeter away from the Si_3N_4's atmospheric face [86].

2.6 Tribology

The triboelectric effect is a type of contact electrification occurring when two objects are brought into contact and then separated. Different mechanisms have been put forth to explain contact electrification for different material types. Electron transfer has been used to explain the cases of metal-metal and metal-semiconductor interaction [87], [88]. Meanwhile, surface states have been used to explain the process in metal-insulator interactions [89]. On the other hand, ion transfer has been put forth to explain the process for metal-polymer and polymer-polymer interactions [90], [91]. Recent work showed that ion transfer does not properly explain the results for inorganic solid contact [92]. Instead, electron transfer appeared to be the dominant process, although ion transfer could happen simultaneously in a minor capacity [92]. From these results, an electron-cloud-potential-well model was proposed to explain contact electrification for all material types [92].

In the electron-cloud-potential-well model, each atom in a material represents a potential well. Electrons reside in the well with the outer electrons towards the top of the well. The well's height represents the potential energy required for electrons to escape. When two materials are brought into contact, the potential wells of two atoms overlap and reduce the potential energy required for electrons to escape the materials' surfaces. At this point, some of the electrons can move between atoms. When the materials are separated, their original potential wells reemerge and the transferred electrons remain with the new atom. This results in a net positive or negative charge developing on the materials. Many other experiments have been conducted that studied the interaction between two particular materials and determined their respective charges after contact. The result is an ordering called the triboelectric series.

The triboelectric series can be qualitatively used to assess whether a material will exit contact with another material with a positive or negative net charge. A few

materials from the series are listed in Figure 4. After two materials come into contact and are separated, the leftmost one will acquire a net positve charge and the rightmost one will acquire a net negative charge. The farther apart the materials are, the greater the magnitude of the charges. The exact results of the interaction can be difficult to quantify because factors such humidity, temperature, surface roughness, applied force, and initial charge can affect the observed results [93]. Zou et al. designed a standardized method with liquid mercury to determine a second material's triboelectric charge density [93]. Their setup controlled for environmental effects by using a glove box and the measurements allowed the team to quantify the triboelectric series. However, when considering an interaction between two of the materials from their quantified series, their results are still best used as a qualitative assessment due to the aforementioned factors.

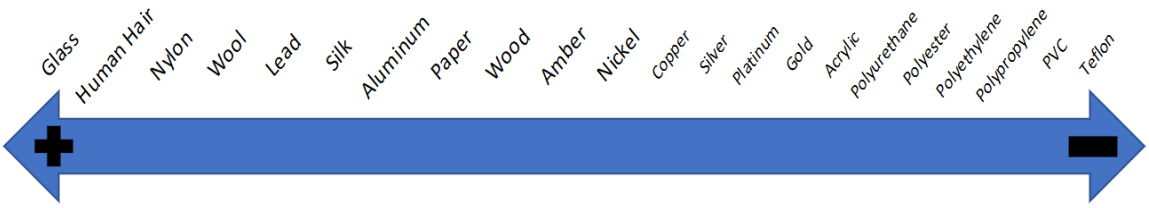

Figure 4. Triboelectric series read from left to right. After two materials come into contact and are separated, the leftmost one acquires a net positve charge and the rightmost one acquires a net negative charge.

2.7 Van de Graaff Generators

Van de Graaff generators are a type of electrostatic generator that were originally developed to accelerate particles to high energies [94], but are now frequently used in classroom environments to teach students about electricity and electrostatic charges. Electrostatic generators are a class of instruments that can produce very high voltages with low currents. A cross-sectional view is shown in Figure 5. Not shown in Figure 5

is the connection between the lower roller and a motor powering the generator. When the generator is operational, a large amount of charge accumulates on the upper dome. In this particular cross-sectional view, the upper dome charges positively and the electrons are routed into ground. Two common demonstrations are stacking tinfoil bowls on top of the dome and having a participant (insulated from the floor) touch the dome. In each demonstration the electric charge travels to the bodies and they repel. Audience members can see the bowls repel each other off of the dome, or all the hairs on the person's head stand up and repel each other. The source of the electric charge is the interaction between the belt and rollers.

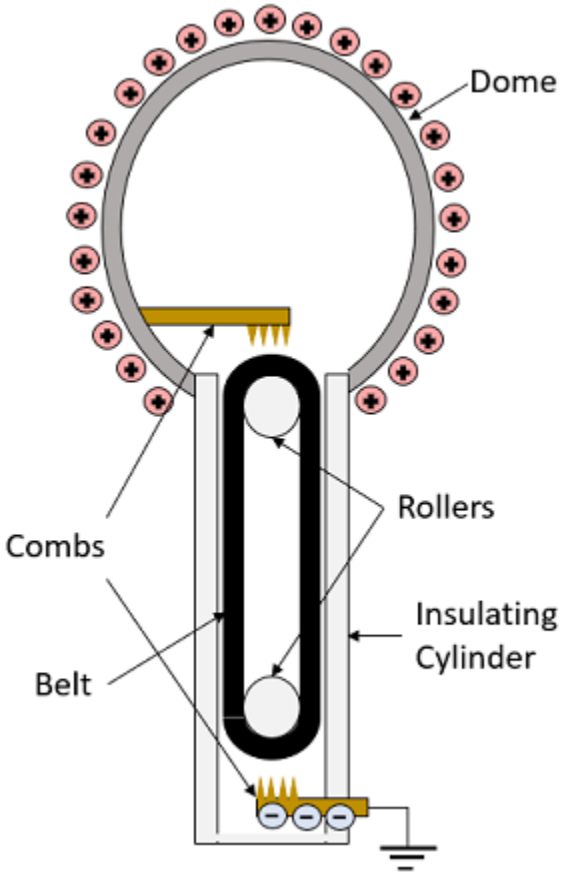

Figure 5. Van de Graaff Generator Cross-Section

When the motor is turned on, the lower roller rotates and pulls the electrically

insulative belt with it. As the belt moves over the roller, the friction between their two materials causes electric charge to be transferred between the two by a process called the triboelectric effect. More information on that can be found in Section 2.6. A similar process occurs when the belt passes over the upper roller. In these interactions, it is the inside of the belt which acquires or loses the electric charge. The materials of the rollers are selected using the triboelectric series such that their interactions with the belt leave the upper one positively charged and the lower one negatively charged. Over the course of many triboelectric interactions between the belt and a roller, a significant amount of charge accumulates on the rollers. Since the total surface areas of the rollers are much less than the belt's, the rollers have much higher surface charge densities and their effect dominates over any differing charge polarity from the belt. The static charges create electric fields originating at each roller. These fields affect the combs, which are typically electrical conductors such as copper, and the air between them.

Air acts as an electrical insulator but it can breakdown and become ionized when affected by a strong enough electric field. This will create a path for charged particles to travel between the belt and the comb. An electric field strength of approximately 30 kV/cm is required to do this at sea level [9]. This value would change if the generator was filled with a different gas. If a net positive charge has built-up on the upper roller, the resulting electric field will attract the electrons from the air onto the belt's outer surface and leave it negatively charged. Meanwhile, the electric field will repel the positively charged air ions towards the conductive comb. When those ions reach the comb, the conductor's electrons will flow to neutralize the ions. Additionally, the positive charge on the upper roller will attract the electrons in the conductor and repel the ions. This will result in a net positive charge on the comb and the metal dome it is attached to. Meanwhile, the lower roller's net negative

charge switches the actions of the electrons and ions. This leaves the lower comb and the attached conductive frame negatively charged. With this separation of charge, a voltage difference develops between the upper and lower conductive elements.

The accumulation of electric charge on a body creates an electric potential relative to other bodies. In the present case, the difference exists between the positively charged dome and the negatively charged base. The exact voltage difference can reach in the hundreds of kilovolts or even into the megavolts depending on the particular construction [94],[95]. These voltage levels exceed the operating ranges for commonly available multimeters, electrostatic voltmeters, and oscilloscopes so it must be measured indirectly. This can be done by connecting the generator's base to another electrode and observing how long of a spark can be created between that and the generator's upper dome [95]. Once the spark length is measured, it can be multiplied by air's breakdown strength to approximately calculate the voltage difference between the two bodies. The voltage will not grow without bound because it is limited by charge leaking into the air when the local electric field is sufficiently large [94]. This can be delayed by designing the generator with a larger dome.

2.8 Summary

This chapter covered potential technologies to remove electric charge from an ungrounded platform such as electrical discharges and thermionic emissions. Corona discharge systems have the most mature aircraft-specific technology. The chapter ended by discussing tribology and Van de Graaff generators to develop an understanding of the research's charge generation method.

III. Methodology

3.1 Overview

This chapter describes the setups and methologies used to test the effects of airflow in removing electrons from an ungrounded body. It starts with testing the small-scale Van de Graaff generator (VdG) and then the full-size VdG. The distances in this section, with the exception of the airfoil's dimensions, are approximations and were found by converting imperial tape measure readings to metric units.

3.2 Small-Scale VdG Testing

3.2.1 Motivation

A small-scale, educational VdG, shown in Figure 6 below, was acquired to practice measuring the voltage drop during a spark discharge between two electrodes. Originally, the practice was done with the full-size VdG, a nearby 41 centimeter diameter aluminum sphere, a 250 Ω resistor, a National Instruments (NI) 9205 card, and a LabView program. However, after the first spark occurred, the software displayed an error message that the card's analog-to-digital converter (ADC) could not switch fast enough. It was believed at the time, incorrectly, that the card's ADC had been permanently damaged because too much current had flown into the card. Using the smaller VdG allowed for the preparation and testing of a circuit that was expected to prevent this scenario.

To avoid damaging further cards, a circuit designed for an unrelated, 10 kV input voltage, higher-power project was adapted and implemented for this experiment. The adapted circuit schematic is shown in Figure 7 below and the components' power ratings are summarized in Table 1 below. Using this circuit with the smaller VdG and measuring the voltage drop across the 8 mΩ resistor still resulted in the same LabView

Figure 6. Small-scale VdG setup used to measure spark discharges. The circuitry is enclosed in the aluminum foil-wrapped cardboard box. This image was taken prior to terminating the coaxial cable with a 46.8 Ω resistor to dampen reflections

error message. The card's 250 kS/s maximum sampling rate was then considered the limiting factor. As a result, the NI card and LabView software were replaced by a Keysight InfiniiVision MSOC3024T Mixed Signal Oscilloscope to achieve higher temporal resolutions.

3.2.2 Setup

The setup used to record the discharges is shown in Figure 6. The wand laying on the cart was brought towards to the VdG's dome to create a five to eight centimeter spark. The aluminum foil wrapping around the cardboard box served as electromagnetic interference (EMI) shielding. The oscilloscope leads were also wound through a ferrite clamp as additional EMI protection. Reflections within the coaxial cables

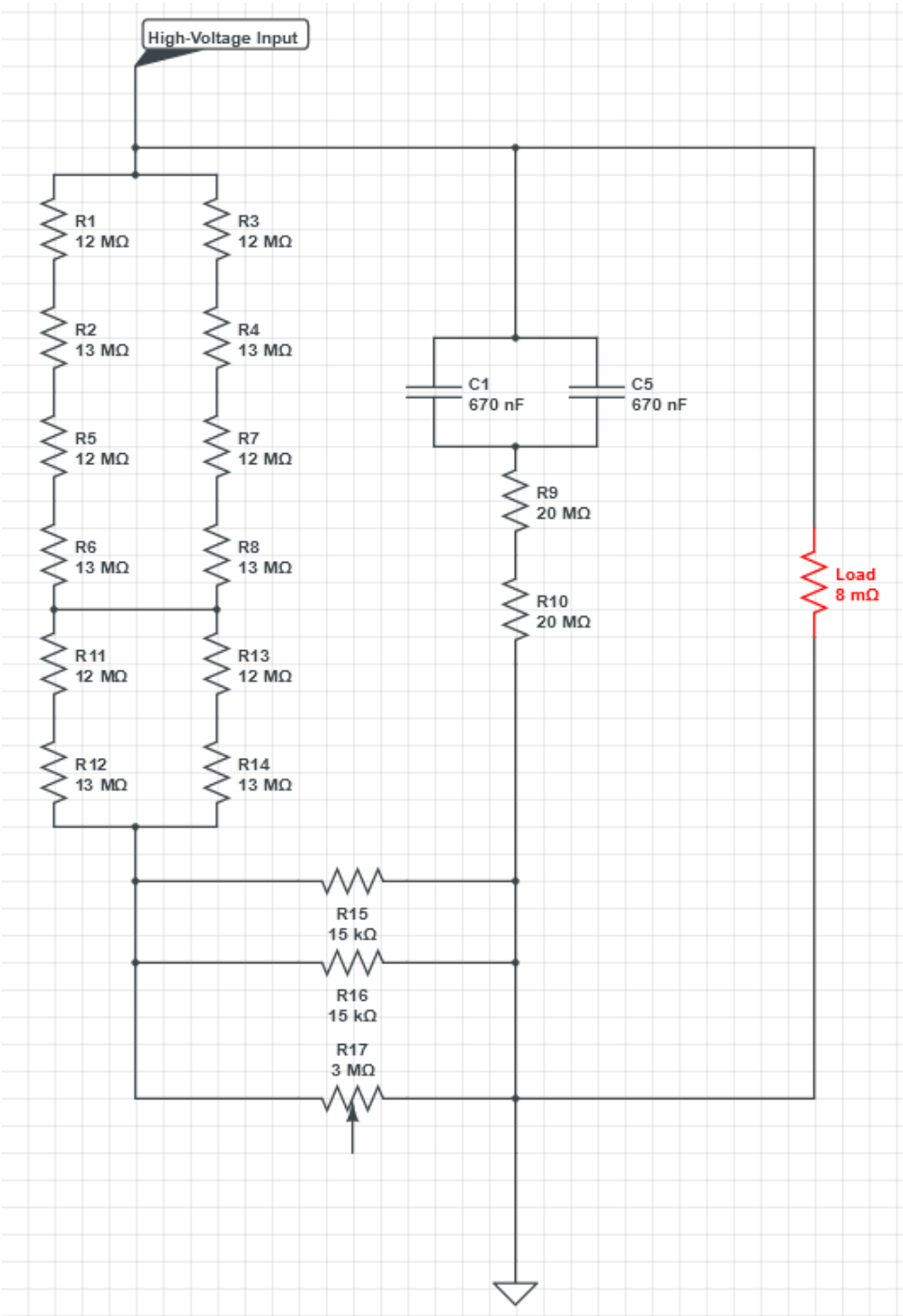

Figure 7. Adapted high-voltage circuit implemented to minimize power dissipated via load resistor during VdG spark discharge. Table 1 contains the component power ratings.

Table 1. Ratings of circuit elements in Figure 7.

Component	Rating
8 mΩ	2 W
5 MΩ pot.	2 W
12 MΩ	2 W
13 MΩ	2 W
20 MΩ	0.5 W
15 kΩ	50 W
0.67 μF	2 kV

were mitigated via a 46.8 Ω termination as is shown in Figure 8 because standard BNC terminators were not available. This value was selected heuristically because the available coaxial cable's relative permittivity was unknown.

Common coaxial cable impedances are 50 Ω and 75 Ω. The available cable was tested with termination impedances of 46.8 Ω, 67.7 Ω, 98.7 Ω, and 0.995 kΩ to assess which best damped reflections. No available resistors were closer to 50 Ω or 75 Ω. The determination was qualitative and based on observing damped harmonic oscillations after a spark [96], [97]. The 46.8 Ω and 67.7 Ω resistors both produced similar waveforms. So, the 46.8 Ω resistor was selected arbitrarily. The VdG produced Radio Frequency (RF) noise regardless if a discharge was occurring.

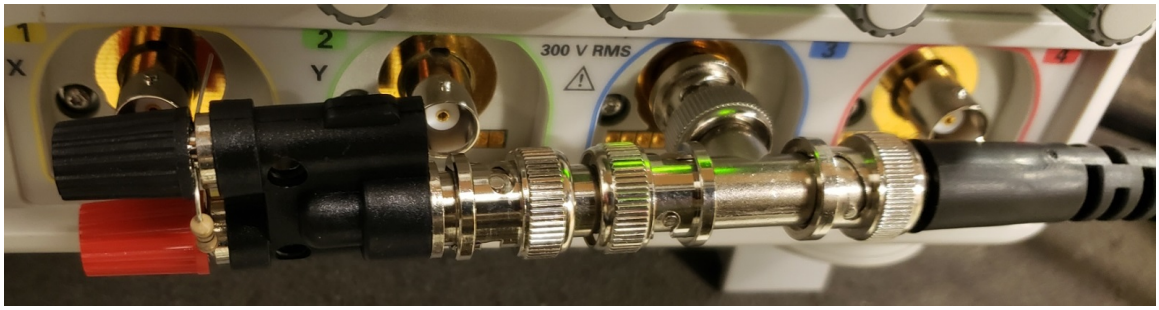

Figure 8. A BNC connector with a 46.8 Ω resistor was used in place of a BNC terminator. Although not ideal, this effectively damped reflections within the coaxial cable.

Once the VdG was turned on, the dome accumulated charge which in turn created an electrostatic field capable of affecting the aluminum discharge wand as the wand was brought closer to initiate a spark. The field caused current to flow through the circuit and produce undesired measurements. Additionally, the discharges themselves were on the order of nanoseconds and the quickly-varying currents in those discharges radiated noise. After implementing the aforementioned EMI countermeasures, sparks consistently produced measurements, such as the two in Figure 9, with forms similar to those observed in [96], [97]. Varying the distance between the oscilloscope and the spark did not noticeably affect the waveforms.

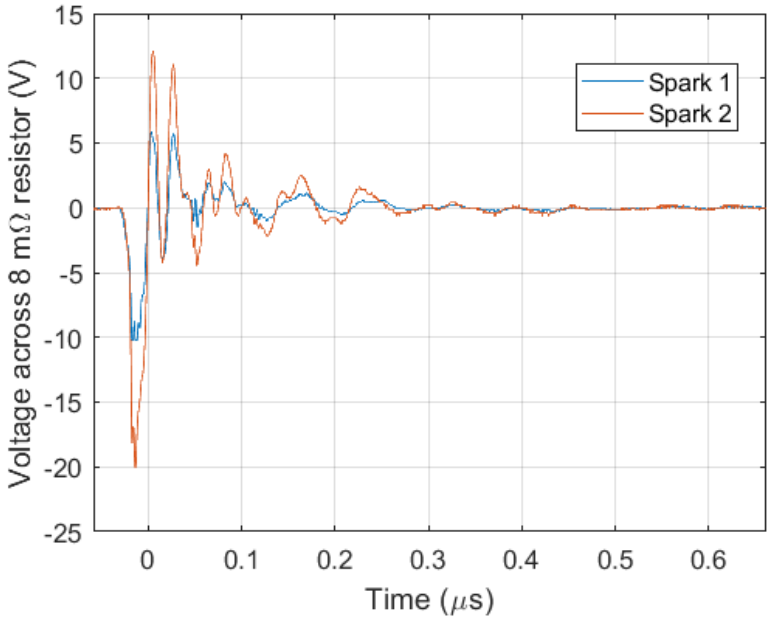

Figure 9. Example waveforms produced by a spark discharge after terminating coaxial cable with a 46.8 Ω resistor. These measurements used the 8 mΩ load resistor in the Figure 7 circuit.

3.2.3 Conclusions

Testing with the small-scale VdG highlighted the importance of EMI shielding and nanosecond temporal resolution in properly recording spark discharges. No readily-

available NI cards offered that resolution and motivated using the oscilloscope for full-scale VdG experiments.

3.3 Full-Size VdG Testing

3.3.1 Overview

Tests with the large VdG assessed the effects of airflow and passive copper wicks on removing electrons from an ungrounded aluminum airfoil. The VdG's rollers were configured to charge the dome positively and the base negatively. The base was then connected through a 0.997 kΩ resistor to the airfoil, which allowed the airfoil to charge negatively. The voltage difference across the resistor was measured and Ohm's law was used to calculate the current flowing through the resistor. This current was also the current leaving the airfoil because, as is shown in Figure 10, the VdG-airfoil setup represented a closed circuit loop. The setup's accuracy, outlined in Section 3.4, was approximately 3.12 mV or 4.26 μA. It was assumed that accuracy errors remained approximately constant while conducting a particular experiment.

3.3.2 Testbed

This section first provides a short overview of the testbed and identifies the key test articles. Following that, the testbed's construction and the key articles are described in detail.

3.3.2.1 Overview

The fully-constructed experimental setup is shown in Figure 11. On the left is a VdG acquired from the Air Force Research Lab (AFRL) and used in previous experiments [96],[97]. To the right of the VdG are the aluminum airfoil in its plexiglass housing, the wooden support structure, and the air blower and stainless-steel ducting.

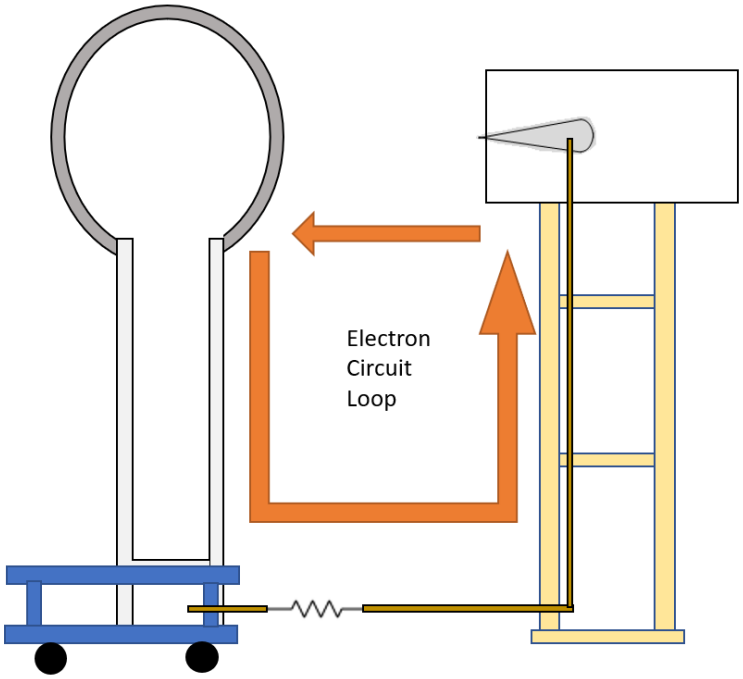

Figure 10. The VdG-Airfoil setup represents a closed circuit loop. The electrons are removed from the VdG's dome, travel down the belt to the VdG's base, flow to the airfoil, and then back to the VdG's dome.

The wooden support structure and ducting were sized and assembled to leave the airfoil's tapered edge approximately 2.286 meters off the ground and level with the VdG's dome's largest radius. This positioning would simplify measuring the spark gap distance if any sparks occurred between the airfoil and dome.

At the bottom of the image is a cardboard box wrapped in aluminum foil. Inside of the box is the resistor whose voltage drop was measured. Originally, the aforementioned 8 mΩ resistor was used. However, that resistor did not produce measurements that noticeably changed when starting and stopping the motor. As a result, it was replaced by a 0.997 kΩ resistor. A VdG may ideally be considered a constant current source, so a larger resistor could make any trends more apparant. To the left of the VdG are an SR560 preamplifer and an oscilloscope. The preamplifer filtered frequencies above 30 Hz from the measured voltages. The SR560's low-pass filter

(LPF) setting was needed because remnants of the 60 Hz power supply were present in the measurements without the SR560. The VdG used a different electrical outlet than the other equipment.

3.3.2.2 VdG

A VdG built by AFRL was acquired and used as this experiment's electrostatic charge source. It had worn down and been collecting dust after previous experiments and needed attention prior to being used again. The lower axle was slightly bent and was straightened out. Additionally, both of the lower axle's endcaps and bearings were replaced. However, these new bearings and endcaps became just as worn down as the originals after several weeks of use.

All surfaces, including the belt and rollers, were dusty and were wiped down using paper towels and soapy water. Two drops of dish soap were added to approximately four to eight liters of warm tap water. The VdG's outer surfaces were dried with paper towels while the inner PVC and belt surfaces were dried by removing the upper dome and flowing air past the exposed top of the belt. The flowing air created suction within the PVC tube and pulled the remaining water out. After cleaning the surfaces, the rollers were oriented to charge the dome positively and the base negatively.

The upper and lower rollers were oriented so that the aluminum roller was on top and the polytetrafluoroethylene (PTFE) roller was on the bottom. This allowed the dome to charge positively and the base to charge negatively. The belt's inner surface had become very smooth due to friction with the two rollers. Consequently, the belt was flipped inside-out so the rougher surface was in contact with the two rollers. Additionally, the aluminum roller's surface was roughened with sandpaper. This increased the touching surface area between the belt and the rollers, which increased the number of triboelectric interactions occurring and therefore the number

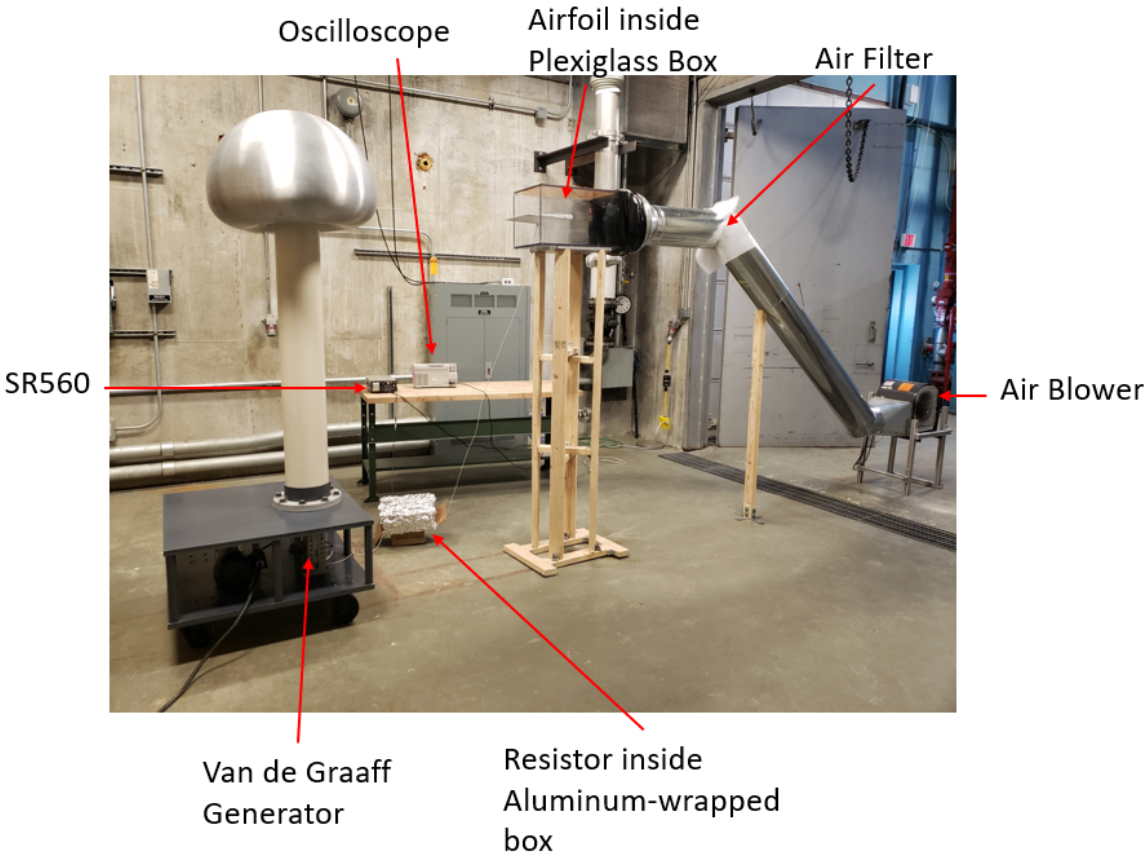

Figure 11. The experimental setup for testing the large VdG.

of electrons generated. The lower roller was originally positioned so that twelve bolt holes were visible below the end caps on each side. This position meant the belt was stretched taut, but not too tightly that the motor had difficulty rotating it. Midway through collecting data, it was noticed that the belt had stretched and become loose around the axles. As a result, the axle was lowered one notch. This did not affect the motor's ability to rotate the axle and belt.

The VdG had a Dayton 3KW97G AC motor spinning the axle and belt. Originally, this motor was connected to an MA7200 Plus General Purpose Drive which in turn was connected to a 208 V, 60 Hz outlet. The VdG ran consistently when setting the drive to frequencies above 40 Hz. The MA7200 was later removed because its operation introduced kHz noise, seen in Figure 12 below, into the voltage measure-

ments that obscured any impact other variables had on the system. The noise was adequately removed by directly connecting the VdG's motor to the power outlet and passing the voltage measurement through the SR560's LPF. Only using the LPF and not removing the MA7200 did not adequately remove the noise. Finally, the grounding cable tied to the rolling platform's underside was connected to the lower comb to consolidate all the generated electrons. The VdG's operation was tested prior to the MA7200's removal using an aluminum strike ball sitting approximately 2.286 m off the ground.

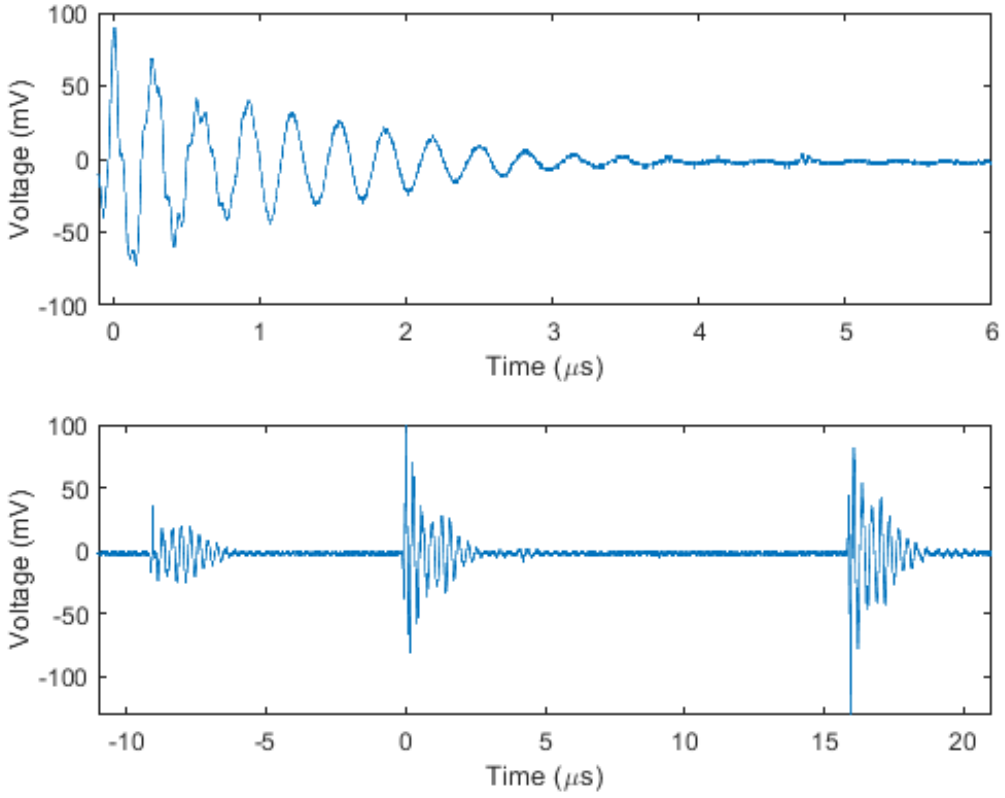

Figure 12. Voltage measurements across 8 mΩ resistor with MA7200 controlling the VdG motor. This noise obscured any effect other variables had on the system. Removing the MA7200 and using a LPF set at 30 Hz cutoff removed this noise as well as traces of the 60 Hz power supply.

The strike ball and its mount, seen in Figure 13 below, were connected to the

VdG's base, electrically floating, and kept off the ground via wooden two-by-four boards. The VdG and strike ball were separated by approximately five to eight centimeters. In order for a spark to cross this gap, a voltage difference, based on an approximate application of Peek's Law, in the upper 100's to lower 200's of kilovolts would be required. Sparks spanning this gap were observed.

Increasing the motor controller frequency from 40, to 50, and finally to 60 Hz made the VdG's belt spin faster and, consequently, decreased the time between sparks. At the 60 Hz setting, the sparks occurred as often as every two seconds. Once the VdG was no longer running, the dome was discharged to the strike ball via the discharge stick shown in Figure 14 below. Moving the strike ball farther away from the VdG did not allow longer sparks to be observed and charge leakage was considered the probable culprit. The test cell was also in use for unrelated experiments and had equipment that formed capacitive relationships with the VdG dome. One alternative explanation was that the electrical insulators within the VdG had degraded and prevented the dome and strike ball from reaching greater voltage differences.

The resistivity of many paths across the VdG were tested with a Megger MIT1525 15 kV insulation tester; the results are summarized in Table 2 below. All measurements indicated that the electrical insulators were still effective. However, those normally insulative surface still became charged after running the VdG for one minute. For example, the outer PVC surface often became charged enough to attract strands of hair and create small sparks to nearby skin.

3.3.2.3 Airfoil

The aluminum airfoil, shown mounted inside its plexiglass container in Figure 11, was teardrop shaped, had a chord length of approximately 30.226 cm, a width of approximately 30.48 cm, and a round edge radius of approximately 1.27 cm. The

Figure 13. Aluminum strike ball

Figure 14. 76.2 cm wingspan discharge stick.

Table 2. Results of testing VdG insulation with Megger MIT1525 did not indicate any electrical insulators had degraded significantly

Red Clamp	Black Clamp	Voltage (kV)	Resistance (TΩ)
PVC Upper Edge	Lower Metal Upright	5	6.21
	Lower Shaft	5	4.68
	Base Nut	5	8.81
Lower Metal Upright	Motor Cable	1	>2
	Strike Ball	1	>2
	Wire to Airfoil	1	>2
Top of VdG Belt	Bottom of VdG Belt	1	>2
Upper Comb	Lower Axle	1	>2

airfoil and plexiglass container were both fabricated by AFIT's model shop. The rectangular plexiglass container was 60.96 cm long and had a 30.48 cm by 30.48 cm opening. The airfoil was mounted inside and vertically centered by four plastic screws. One of the plastic screws was replaced by a metal screw and a wire to connect the VdG and airfoil. Additionally, aluminum plates were added to both the bottom of the plexiglass and the top of the wooden support structure that fit together for an easier and more secure mounting. Eventually, the airfoil's outer surface was coated with VHT Engine Enamel, which is a ceramic formula, to test the effect of an insulating layer. The VHT-coated airfoil is visible in Figure 15 below. A multimeter confirmed the layer was effective.

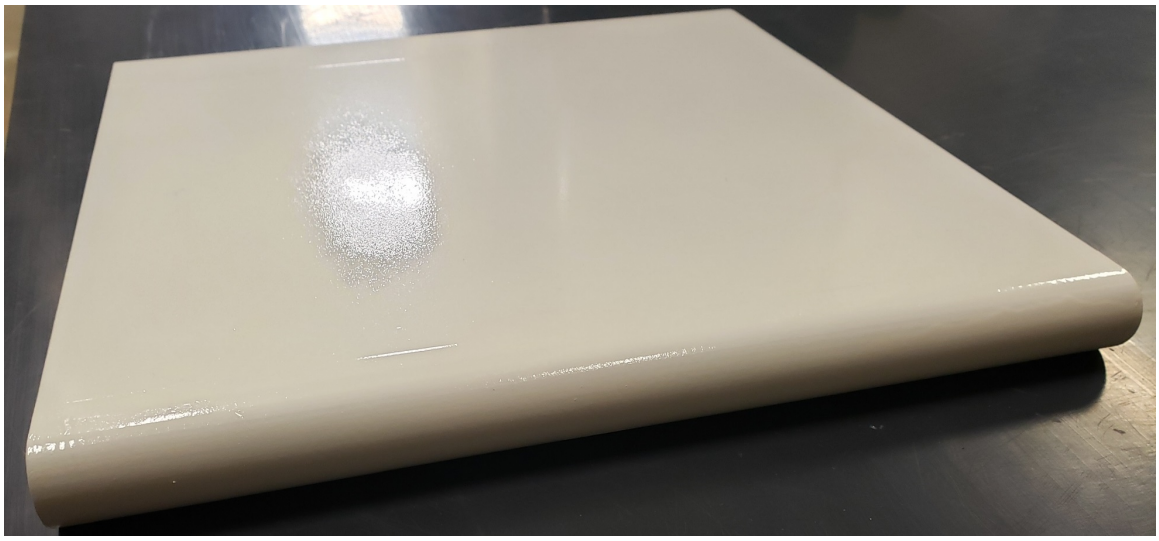

Figure 15. Airfoil after being coated with a ceramic engine enamel spray paint.

3.3.2.4 Wind Tunnel

The wind tunnel was built using a Dayton Blower 1XJY2A and stainless steel ducting. The fabric extending out of the ducting in Figure 11 is a Pamlico Air fiberglass FPR 1 air filter added to provide more uniform airflow speeds across the

entire cross-section. This came at the expense of reduced air speed. Preliminary tests at the motor's highest setting, before inserting the filter, had the handheld Extech Instruments model 407123 hot wire thermo-anemometer commonly exceeding its 20 m/s limit and fluctuating significantly.

After inserting the filter, the measured speeds were approximately halved, as can be seen in the velocity profile shown below in Figure 16. The anemometer did not have a connection port to export wind speeds to a computer. As a result, velocities shown at the tick mark intersections in the profile resulted from mentally averaging the observed speeds. No measurements were taken at the 15.24 cm vertical tick because the airfoil occupied that space. No measurements were taken at the outer edges. The profile could have been more uniform if additional ducting was added after the filter. Space constraints prevented doing so.

A rule of thumb is laminar flow requires the length of straight ducting to be ten times the duct's diameter. The ducting had a diameter of approximately 25.4 cm but there was only 129.54 cm of ducting between the filter and the airfoil's round edge. The air flown over the airfoil was ambient air which, depending on the time of day, measured between 14 and 22 degrees Celsius and 16 to 28 percent relative humidity. The air temperature and relative humidity were monitored with an AcuRite digital thermometer and humidity gauge.

3.3.2.5 SR560 Preamplifier

Measuring the voltage drop across the 0.997 kΩ resistor and sending the signal straight to the oscilloscope resulted in noisy data that showed traces of the 60 Hz power supply signal. To filter out the higher-frequencies, an SR560 low noise voltage preamplifier was used. It was configured to read in a single signal with DC coupling, apply a low-pass filter with a cutoff frequency of 30 Hz with a 6 db/oct rolloff, then

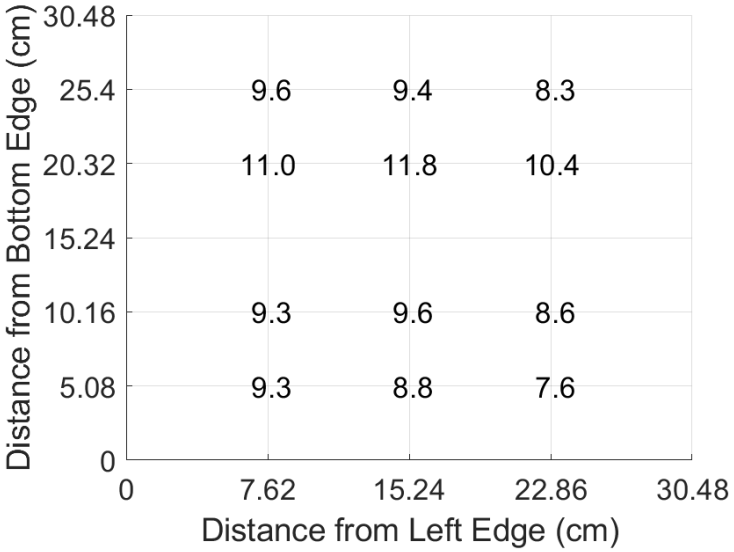

Figure 16. Velocity (m/s) profile of blower at highest setting after adding in the air filter. The values resulted from mentally averaging the anemometer's readings with the sensor at each position. Measurements were not taken at the 15.24 cm height because the airfoil was there.

amplify the measured signal by 10. It was not noticed until after spray painting the airfoil that a ten-times amplification was not being provided. This was a scaling issue and was accounted for by using a DC power supply to calculate the true gain experienced.

The SR560 had 600 Ω and 50 Ω output connectors. The 600 Ω output was used because the manual indicated that using the output corresponding to the load's resistance would halve the gain provided. A BK Precision 9121A DC power supply was used with the SR560 to determine the exact gain from the preamplifier. Sending 200±2.04 mV and 400±2.08 mV signals from the power supply into the SR560 with the aforementioned configuration produced DC signals with gains of approximately 0.734. The SR560's 50 Ω output did amplify the signal but remained unused to maintain procedural consistency. When using the SR560, a high dynamic reserve gain mode was used to apply the gain at the filter's output stages and prevent overloading

the amplifier.

One downside to the SR560 is that it can only handle an input DC voltage of one volt before being thrown into a persistent overload state. Overloads always happened when not disconnecting the SR560's input coaxial cable before discharging the VdG and airfoil. The SR560 manual identified the front-end FET (U106, P/N NPD5564), as the likely damaged component. However, the two SR560s which were in the persistent overload state and opened up had LSK389 JFETs instead. Replacing the LSK389s fixed the persistent overload states. The NPD5564 and LSK389 were not readily available from local electronics stores and great care should be taken to avoid damaging the SR560.

3.3.3 Determining VdG Dome-to-Airfoil Spacing

The research's objective was to determine how airflow affected the current leaving a charged ungrounded body. This meant that the VdG-airfoil separation distance needed to be large enough to make the VdG dome's electrostatic field's impact as small as possible. The first experiment performed assessed different spacings both with and without air flowing over the airfoil.

The testbed was positioned so that the VdG sat in the middle of the room. This was done to reduce charge leakage to objects and surfaces unrelated to the experiment. The airfoil and wind tunnel were moved and extended out of the test cell. While moving the wind tunnel, the ducting connecting to the blower came off. To prevent this happening again whenever a different VdG-airfoil spacing was tested, the airfoil and wind tunnel were positioned so that when the VdG sat in the center of the room and there was a 76.2 cm air gap between the dome's largest radius and the airfoil's tapered edge. Then, for a particular spacing, the VdG was moved towards the airfoil.

All spacings tested and their randomly generated test order are shown in Table

3 below. Distances greater than 76.2 cm were not considered due to the discharge stick's size. Once the VdG dome and airfoil were separated the desired amount, six total runs – three with air flowing and three without air flowing – were performed before changing the spacing. The orders of those six runs for each spacing are also shown in Table 3 below.

The VdG ran for at least one minute each run. Some runs lasted a few seconds longer than others because, due to removing the motor's frequency drive, the electrical control box's lever needed to be thrown to turn the motor on and off. After the minute had passed and the motor had stopped, the SR560 was turned off and its input coaxial cable was disconnected. Then, the discharge stick was used to connect the airfoil to the dome and discharge the two objects. Next, the VdG was repositioned if necessary and the dome was reseated. The VdG vibrated while running and the dome sometimes became lopsided and needed to be reseated. After those steps, the run's data was saved, the SR560 was turned on and the input coaxial cord was reconnected, and the blower setting was adjusted if needed. Analysis of the average current flowing from 20 to 50 seconds after the motor started, see Section 4.3, indicated the 76.2 cm spacing was suitable and therefore used to test the effects of adding copper wicks to the airfoil. At that spacing, the sample averages of the just-mentioned average current appeared settled within an approximately 1 μA range and the variance was less than 0.037 μA^2.

3.3.4 Adding Copper Wicks to Airfoil

After a 76.2 cm spacing between the VdG dome and the airfoil's tapered edge was determined to be suitably far, the effects of adding up to three copper wicks to the unpainted tapered edge were assessed. The wicks were made from completely stripped segments of 12 AWG copper wire and positioned to extended 7.62 cm past

Table 3. Testing order for different VdG dome and airfoil tapered edge spacings. All blower setting runs at a spacing were completed before moving the VdG again. The spacing test order and blower setting orders were generated randomly.

Spacing (cm)	Test Order	Blower Setting Order					
2.54	3	On	Off	Off	Off	On	On
7.62	5	On	Off	Off	On	On	Off
15.24	7	On	Off	Off	On	On	Off
22.86	11	Off	On	Off	On	Off	On
30.48	2	On	On	Off	Off	On	Off
38.10	4	On	On	On	Off	Off	Off
45.72	1	Off	On	On	On	Off	Off
53.34	8	On	On	Off	On	Off	Off
60.96	9	On	On	Off	On	Off	Off
68.58	10	On	On	Off	On	Off	Off
76.20	6	Off	On	Off	Off	On	On

the tapered edge. To create additional sharp points for charge to leak from, the copper strands at the end extending past the edge were spread out parallel to the edge and covered a distance of 2.54 cm. The case of three wicks spaced out 7.62 cm is shown in Figure 17 below. The test procedure was nearly identical to that used when determining the appropriate spacing. However, the VdG was not moved and only the wick arrangement was modified. The run orders for each wick arrangement and spacing are shown in Table 4 below.

In addition to adding wicks and observing the results, the spacing between wicks was also considered in the case of two wicks. Introducing additional wicks introduces additional locations for charge to flow through. As the charge leaves the wick and travels to the VdG it accumulates as regions of space charge in the air. These regions will have their own electric field and may interact with the other wicks and hinder charge leaving from those wicks. The spacing between wicks was varied to identify a distance where the wicks did not interact with each other. Tests with two wicks

Figure 17. Airfoil with three copper wicks attached to the tapered edge with an inter-wick spacing of 7.62 cm. All wicks extend 7.62 cm past the edge.

Table 4. Run order for attaching wick configurations to the aluminum airfoil. Only the blower setting orders were randomized. All blower setting runs for a wick setup were completed before changing the wick setup.

Wick Amount	Wick Spacing (cm)	Test Order	Blower Setting Order					
0	N/A	1	Off	On	Off	Off	On	On
1	N/A	2	On	On	Off	On	Off	On
2	2.54	3	On	On	On	Off	Off	Off
	5.08	4	On	On	Off	Off	On	Off
	7.62	5	Off	On	On	On	Off	Off
3	7.62	6	On	On	Off	Off	On	Off

indicated spacing them out by 7.62 cm was acceptable. Therefore, when the third wick was added it was placed 7.62 cm away.

3.3.5 Coating Airfoil with Electrically Insulating Paint

Following the copper wick tests, the airfoil's outer surface was spray painted with a ceramic VHT engine enamel to create an electrically insulating layer. This paint was verified by using a Fluke 179 multimeter to measure the resistance of both a metallic object previously coated with it and the airfoil. The same wick-varying procedure was used to test the insulated airfoil and the run order is shown in Table 5 below.

3.4 Measurement Accuracy

This section discusses and calculates the measurement errors due to the SR560 preamplifier and the Keysight InfiniiVision MSOC3024T Mixed Signal Oscilloscope. It then converts the total voltage accuracy to a current accuracy. The section then discusses the accuracy assumptions inherent in the analysis of Chapter 4.

Table 5. Run order for attaching wick configurations to the insulated airfoil. Only the blower setting orders were randomized. All blower setting runs for a wick setup were completed before changing the wick setup.

Wick Amount	Wick Spacing (cm)	Test Order	Blower Setting Order					
0	N/A	1	On	On	On	Off	Off	Off
1	N/A	2	Off	Off	On	On	Off	On
2	2.54	3	On	Off	Off	On	Off	On
	5.08	4	Off	On	On	On	Off	Off
	7.62	5	On	Off	On	Off	Off	On
3	7.62	6	On	Off	On	On	Off	Off

3.4.1 SR560 Accuracy

The SR560 was configured to provide a gain of 10 in the High Dynamic Reserver (HDR) mode. The SR560's Noise Figure (NF) was defined by Equation 8 [98]:

$$\text{NF} = 20 \log_{10} \left(\frac{\text{Output Noise}}{\text{Gain} \times \text{Source Thermal Noise}} \right). \tag{8}$$

Solving for the output noise produces Equation 9:

$$\text{Output Noise} = \text{Gain} \times \text{Source Thermal Noise} \times 10^{\text{NF}/20} \tag{9}$$

The gain was calculated to be 0.734 (see Section 3.3.2.5), the NF was estimated from noise contours in the SR560's manual (reproduced in Figure 18), and the thermal noise was calculated via Equation 10:

$$V_n = \sqrt{4 k_b T R \Delta f} \tag{10}$$

where V_n is the thermal noise in Volts, k_b is the Boltzmann constant (1.380649×10^{-23} J/K, T is the temperature in Kelvin, R is the resistance (997 Ω), and Δf is the SR560's bandwidth (30 Hz). The highest temperature recorded was 295 Kelvin and resulted in approximately 22 nV of thermal noise. The NF estimate ranged from 20 to 5 dB, corresponding to DC and 30 Hz respectively. Using the calulated thermal noise, the measured 0.734 gain, and the 20 and 5 dB NF estimates resulted in between 22 and 162 nV of output noise with higher amounts at lower frequencies.

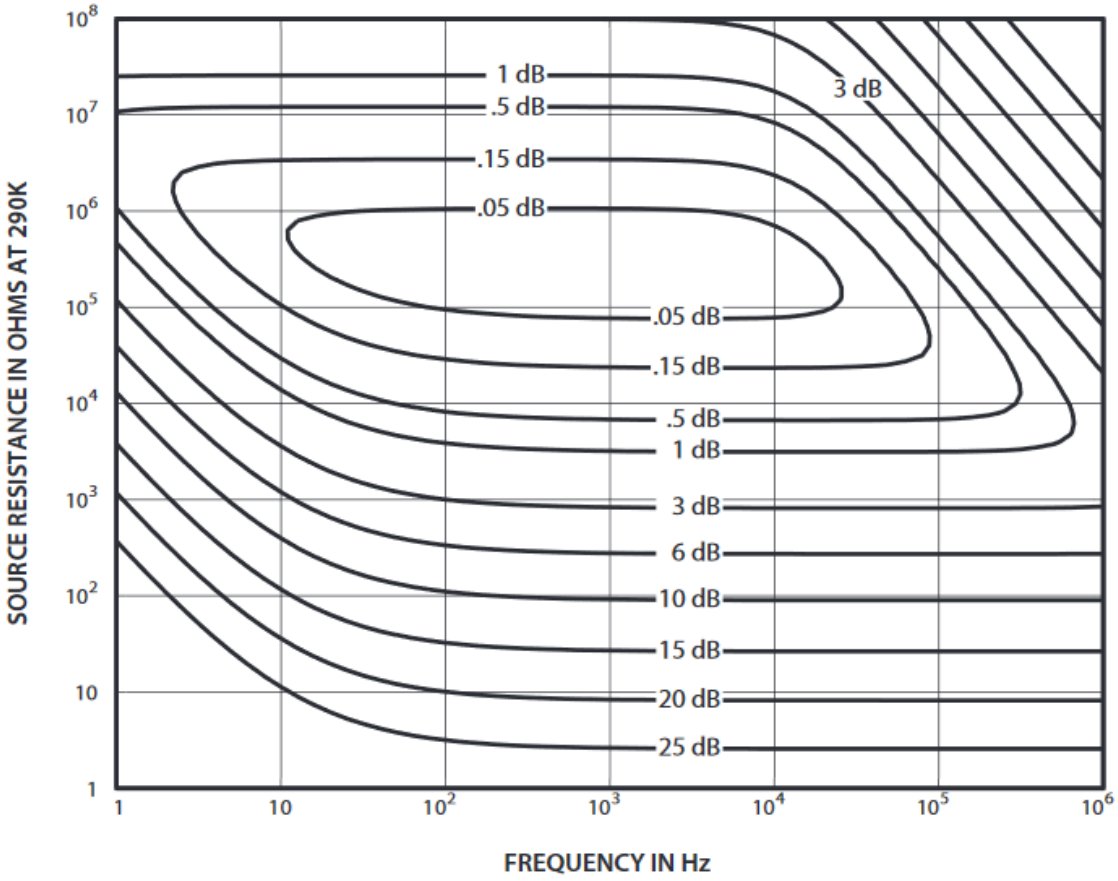

Figure 18. SR560's noise contours

3.4.2 Oscilloscope Accuracy

The Keysight InfiniiVision MSOC3024T Mixed Signal Oscilloscope's DC vertical accuracy is defined by Equation 11 below [99]:

$$A_{\text{Vert}} = \pm[A_{\text{VertGain}} + A_{\text{VertOffset}} + 0.25\% \text{ Full-Scale}] \tag{11}$$

where A_{VertGain} is the DC vertical gain accuracy, $A_{\text{VertOffset}}$ is the DC vertical offset accuracy, and Full-Scale is the total vertical range displayed. The DC vertical gain accuracy is calculated via Equation 12:

$$A_{\text{VertGain}} = 2.0\% \text{ Full-Scale} \tag{12}$$

while the DC vertical offset accuracy is calculated via Equation 13:

$$A_{\text{VertOffset}} = 0.1 \text{ div} + 2 \text{ mV} + 1\% \text{ offset setting} \tag{13}$$

where div is the vertical increment per division, and offset setting is the vertical offset. The settings used were: 32 mV full-scale, 4 mV/div, and 0 mV offset. When using these values in prior equations, the DC vertical gain accuracy was calculated to be ± 0.64 mV, the DC vertical offset accuracy was calculated to be ± 2.4 mV, and the DC vertical accuracy was calculated to be ± 3.12 mV.

3.4.3 Total Accuracy

The SR560's maximum accuracy was ± 162 nV and the oscilloscope's accuracy was ± 3.12 mV. Since 3.12 mV $\gg$ 162 nV, the total accuracy between the two stages was approximated as 3.12 mV. Dividing by the measured resistance (997 Ω) and measured gain (0.734) produced an accuracy of approximately 4.26 μA. It was assumed that accuracy errors remained approximately constant throughout each experiment.

3.5 Summary

This chapter described the setups and methologies used to test the effects of airflow in removing electrons from an ungrounded body. It started with testing the small-scale VdG and then the full-size VdG. The small-scale tests provided familiarity with spark discharges. The full-size tests established an appropriate VdG-airfoil spacing and assessed the effect of airflow on conductive and insulative airfoils with various wick arrays attached.

IV. Analysis

4.1 Overview

This chapter analyzes the results of the experiments performed using the larger, full-size Van de Graaff generator (VdG) described in Section 3.3. First, the VdG-airfoil spacing results are discussed. Following that are the consequences of adding passive copper wicks to the aluminum airfoil. Finally, the chapter discusses the trends observed after coating the aluminum airfoil with a ceramic engine enamel that was an electrical insulator. As mentioned in the previous chapter, the distances in this section were found by converting imperial tape measure readings to metric units.

Before discussing the experiment results, it is worth discussing some observations regarding a VdG's output. In short, Van de Graaff generators are highly variable machines. The measurements they generate may vary between days, successive trials, or even during the current trial. The measurements for each experiment are self-consistent, but comparing particular current levels between experiments - especially those ran on different days - is not always a straightforward comparison. The extent to which the current can suddenly change will become evident after analyzing all the upcoming plots.

4.2 Data Conditioning

Although voltage measurements were taken, the current flowing through the airfoil was desired. The voltage measurements were converted to current measurements by applying Ohm's law and dividing by the measured SR560 gain:

$$I = \frac{V}{997\Omega * 0.734} \tag{14}$$

where I is the current, V is the voltage (pre-filter), 997Ω is the measured resistance value, and 0.734 is the measured SR560 gain. The current measurements were highly variable; however, they still showed an underlying trend. Events such as the VdG motor starting and stopping could easily be identified in all curves. In order to isolate those trends, a moving average filter was applied. The filter used a 750 sample window, selected heuristically, and gave each sample uniform weighting. An example of the raw and filtered data are shown in Figure 19 below. This same procedure was applied to all data sets recorded.

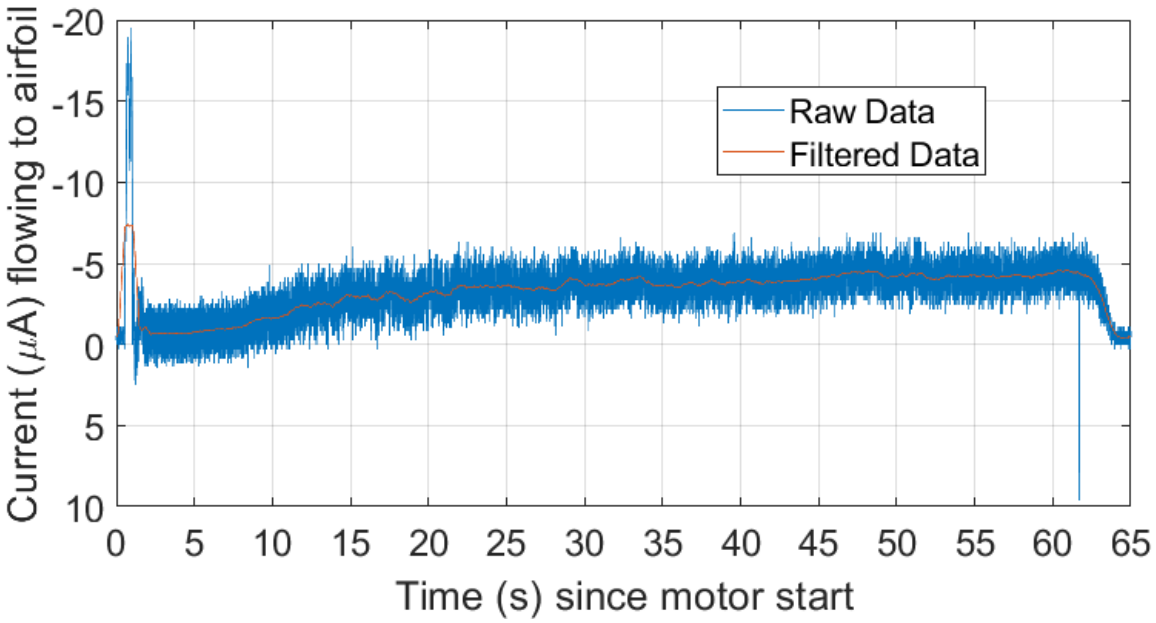

Figure 19. Passing raw data through a moving average filter using 750 uniformly weighted samples extracted the DC component

4.3 Determining VdG Dome-to-Airfoil Spacing

The currents measured for each VdG-Airfoil spacing and airflow setting combination are shown in Figures 20 and 21. The currents are on the order of μA which corresponds to voltages on the order of mV. The currents are negative because the

VdG's rollers were configured to have electrons flow out the base to the airfoil.

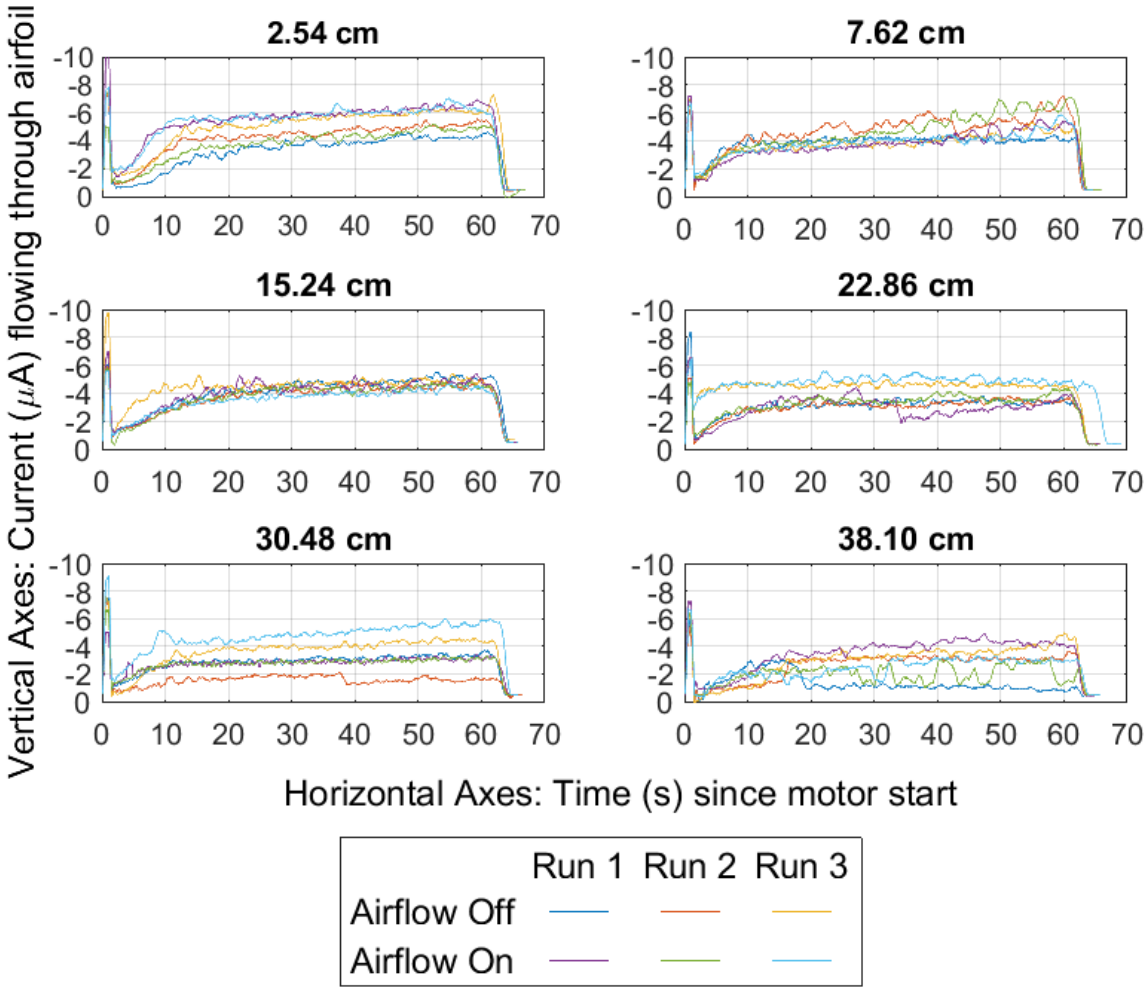

Figure 20. Current (μA) flowing through the airfoil as a function of time (s) since starting the VdG's motor at VdG-airfoil spacings from 2.54 to 38.1 cm. A moving average filter using 750 uniformly weighted samples was applied.

Regardless of the spacing tested, all current measurements had three commonalities. First: a quick spike as the VdG was turned on followed by a return to near-zero current. After that, the current increased to a relatively steady limiting value. While some spacings showed consistent rise times across the different runs, such as 68.58 cm in Figure 21, others, such as 2.54 cm in Figure 20, did not. Finally, all currents

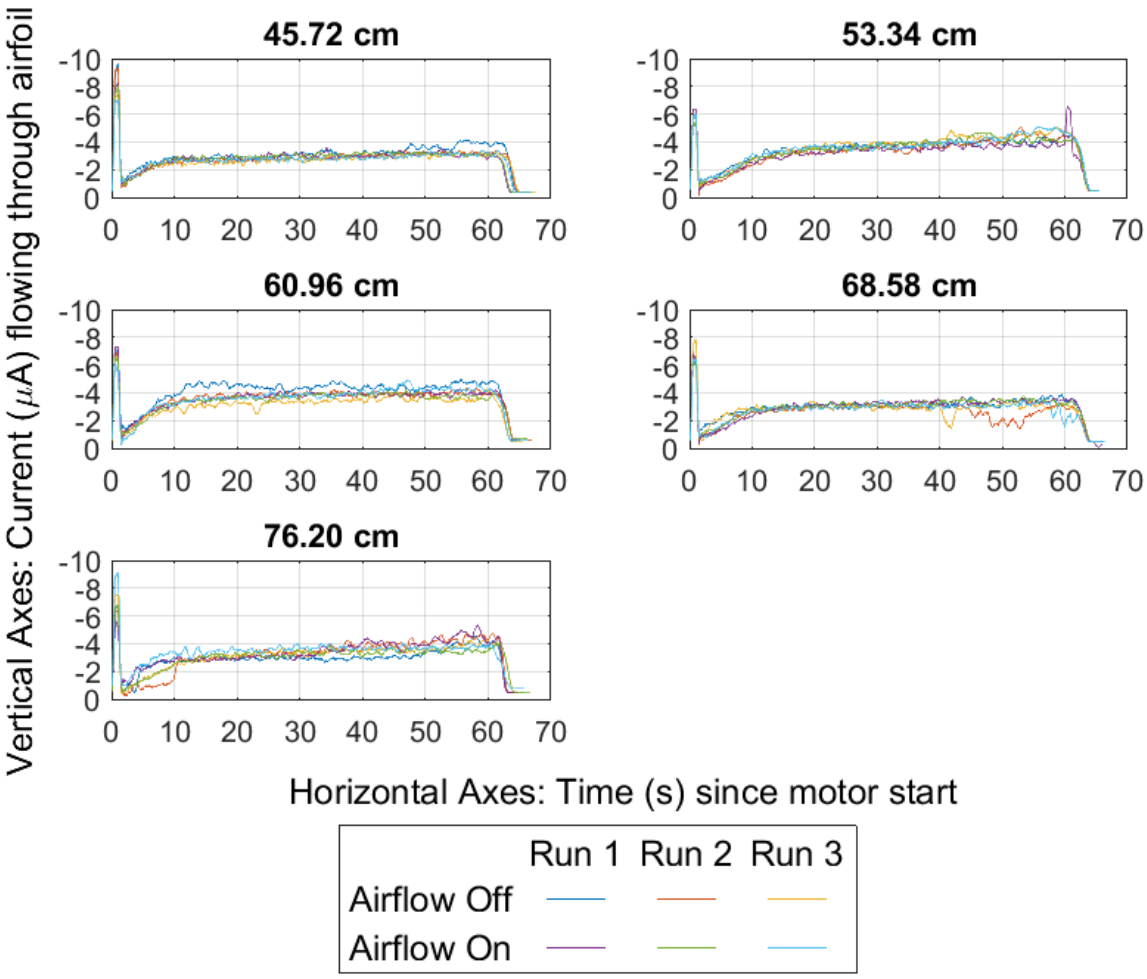

Figure 21. Current (μA) flowing through the airfoil as a function of time (s) since starting the VdG's motor at VdG-airfoil spacings from 45.72 to 76.2 cm. A moving average filter using 750 uniformly weighted samples was applied.

dropped back to pre-VdG start levels after the VdG was turned off. The VdG turning off is identified by each curve's descent after 60 seconds. While those commonalities existed across runs, significant differences were apparent too. The most apparent difference was the limiting current achieved.

4.3.1 Limiting Currents

Qualitative assessments of the filtered data were used to evaluate when each curve had reached a limiting current. Filtered data limiting values were typically reached and maintained between 20 and 50 seconds after the motor's start. Some measurements, such as the second airflow on run for the 38.10 cm subplot in Figure 20, did fluctuate during this time window. However, the window was still deemed appropriate because an inability to reach a consistent limiting current was a behavior of interest. The term "limiting current" is defined henceforth to be the average current measured from 20 seconds to 50 seconds after the motor started and is denoted by I_{L}. Only limiting currents of filtered data were used because the greatest percent difference magnitude between limiting currents of filtered and raw data was 0.1241%. The percent differences were calculated using Equation 15:

$$\%\ \text{Difference} = \frac{I_{\mathrm{L,Filtered}} - I_{\mathrm{L,Raw}}}{I_{\mathrm{L,Raw}}} * 100\% \tag{15}$$

where $I_{\mathrm{L,Filtered}}$ and $I_{\mathrm{L,Raw}}$ were the limiting currents of the filtered and raw data respectively.

The limiting currents for each filtered set of measurements are shown in Table 6 below. The $\hat{\mu}$ sample averages of the limiting currents are plotted below in Figure 22 with 95% confidence interval error bars. The upper and lower bounds for each interval are listed in Table 7. The confidence intervals for the individual airflow settings (on and off) used t-distributions with two degrees of freedom.

The separation distance noticeably affected the limiting currents and confidence interval widths. From 2.54 cm through 38.10 cm on Figure 22 the limiting current decreased nearly linearly. However, the confidence intervals for those distances, except the 15.24 cm confidence interval, indicated uncertainties exceeding 2 μA. After the

Table 6. Limiting currents for each VdG-Airfoil separation distance and airflow combinations. The values in each *Run* column were calculated by averaging the filtered current measurements from 20 to 50 seconds. The $\hat{\mu}$ columns are sample means of the limiting currents indicated by the subscript.

Spacing (cm)	Limiting Current (μA)							
	Airflow Off				Airflow On			
	Run 1	Run 2	Run 3	$\hat{\mu}_{\text{off}}$	Run 1	Run 2	Run 3	$\hat{\mu}_{\text{on}}$
2.54	-3.802	-4.594	-5.558	-4.651	-5.922	-4.173	-5.897	-5.330
7.62	-4.107	-5.145	-3.929	-4.394	-3.916	-4.874	-4.009	-4.267
15.24	-4.577	-4.256	-4.691	-4.508	-4.461	-4.240	-3.880	-4.194
22.86	-3.339	-3.219	-4.611	-3.723	-3.026	-3.585	-5.066	-3.892
30.48	-3.054	-1.682	-4.002	-2.913	-2.898	-2.882	-4.935	-3.571
38.10	-1.080	-3.105	-3.400	-2.528	-4.067	-1.974	-2.642	-2.895
45.72	-3.138	-2.923	-2.801	-2.954	-2.997	-3.062	-2.821	-2.960
53.34	-3.806	-3.613	-4.006	-3.808	-3.545	-3.894	-3.802	-3.747
60.96	-4.391	-3.889	-3.415	-3.899	-3.856	-3.808	-3.966	-3.877
68.58	-3.125	-2.880	-2.897	-2.967	-3.269	-3.228	-3.022	-3.173
76.20	-2.973	-3.617	-3.431	-3.340	-3.509	-3.318	-3.651	-3.493

Table 7. Upper and lower bounds for the 95% confidence interval error bars displayed in Figure 22

Spacing (cm)	95% Confidence Interval Bounds (μA)			
	Airflow Off		Airflow On	
	Upper	Lower	Upper	Lower
2.54	-6.836	-2.466	-7.821	-2.840
7.62	-6.025	-2.762	-5.579	-2.954
15.24	-5.068	-3.948	-4.921	-3.466
22.86	-5.640	-1.807	-6.510	-1.274
30.48	-5.811	-0.015	-6.505	-0.638
38.10	-5.667	0.610	-5.550	-0.239
45.72	-3.378	-2.530	-3.270	-2.650
53.34	-4.296	-3.320	-4.197	-3.297
60.96	-5.111	-2.686	-4.077	-3.676
68.58	-3.306	-2.628	-3.501	-2.844
76.20	-4.163	-2.518	-3.907	-3.078

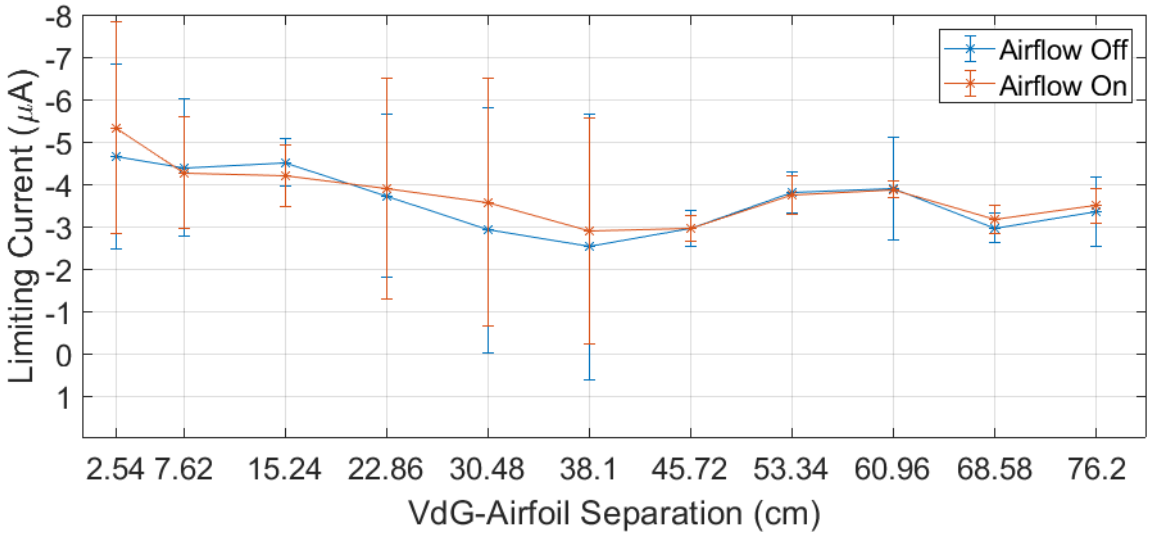

Figure 22. Sample averages of the limiting currents listed in Table 6 with 95% confidence interval error bars added. Confidence interval bounds are listed in Table 7

38.10 cm markers, the limiting current increased to 22.86 cm and 30.48 cm levels but with lower variability. These trends were likely due to the VdG's dome's electrostatic field.

The VdG's dome charged positively and exerted an attractive force on the negatively charged airfoil. At shorter distances, a larger voltage gradient existed between the two bodies. Consequently, the electrons on the airfoil experienced a greater attractive force and a larger current was measured. The variability came from both the inherent variability in a VdG as well as the non-uniformity in the dome's electric field. The variance in limiting currents showed greater dependence on the airfoil and VdG being closer than the order spacings were tested, as can be seen in Figure 23 below.

Based on the limiting currents, the VdG was positioned to have 76.2 cm separating it and the airfoil when adding copper wicks. This was done because the wicks extended 7.62 cm past the airfoil's edge, putting them 68.58 cm from the VdG. In addition to the

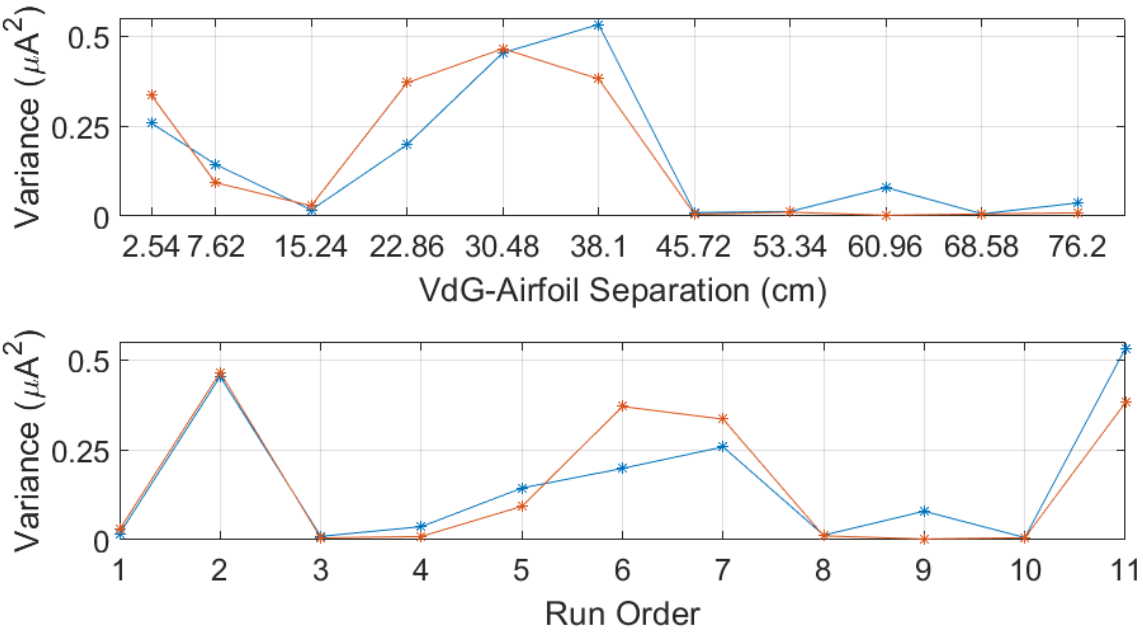

Figure 23. Variance of limiting current measurements as functions of VdG-Airfoil separation distances and spacing run orders.

low current and variability at that distance, the dome's electric field was considered to have decayed enough to not significantly impact the current flowing out of the airfoil. The air blower being on or off did not weigh into the determination based on the consistent overlap between the curves and confidence intervals in Figure 22.

Later, after testing the copper wicks, the VdG's base was disconnected from the airfoil and, still with the resistor, connected to a grounding strip. These measurements characterized the current flow without the VdG dome-airfoil interaction. The results are shown in Figure 24 below. The current magnitude is not relevant to the earlier measurements because, as will be discussed in Section 4.4, a step-function-like jump occurred unexpectedly and became persistent. The curve's form is still relevant: the spike with the motor starting, the rise to a limiting current, and finally a steep decline after turning the motor off. The appearance of these components while the airfoil was removed from the circuit indicate that they are likely byproducts of the

VdG's construction and operation. The ramp-up and level off potentially indicate an ionization and subsequent saturation of air gaps between the combs and belts.

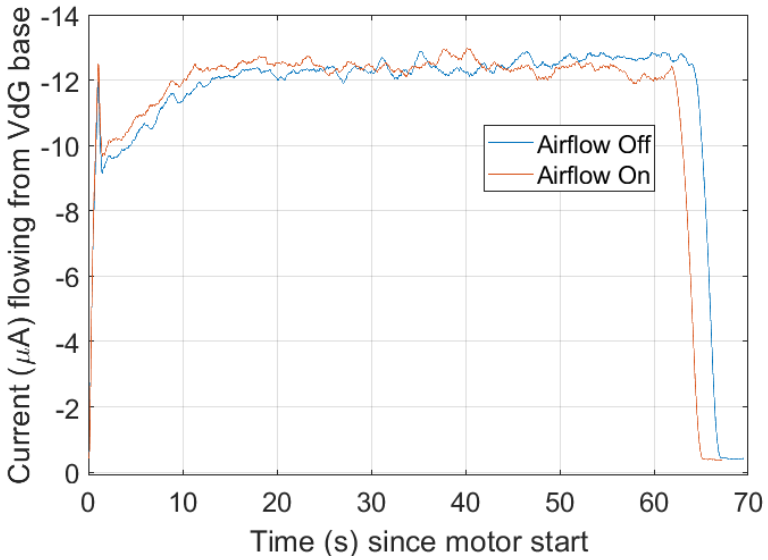

Figure 24. Current (μA) flowing out of the VdG's base, through a 0.977 kΩ resistor, into a ground strip as a function of time (s) since the motor started. The airfoil was not attached to the base. A moving average filter using 750 uniformly weighted samples was applied.

4.3.2 Spectral Analysis

Spectral analysis of the current measurements was conducted to identify dominant components. This analysis was only performed on the data in the 20 to 50 second window based on Figure 24's indication the sharp spike, ramp up, and steep decline were not introduced by the airfoil. The SR560's cutoff frequency and rolloff were set at 30 Hz and 6 dB/oct respectively during data collection. These settings were selected to filter out noise from the VdG's supply power without eliminating the potential to observe any unexpected elements.

The first spectrum considered was the grounded case considered at the end of Section 4.3.1 to ascertain what frequencies could potentially be attributed to the

VdG's operation. The one sided spectrums are shown overlain in Figure 25 below. The left subplot shows the raw data spectrums. Those were nearly identical and had peaks at DC and approximately 65 Hz. The DC component is reasonable because a VdG may be ideally considered a constant current source. The 65 Hz component is nearly a discrete impulse. This indicates it may potentially be an effect of the VdG motor's input 60 Hz signal propagating through the system. The right subplot shows the spectrum after subtracting the raw data's mean from the raw data. It highlighted that most higher frequency peaks were harmonics of 65 Hz.

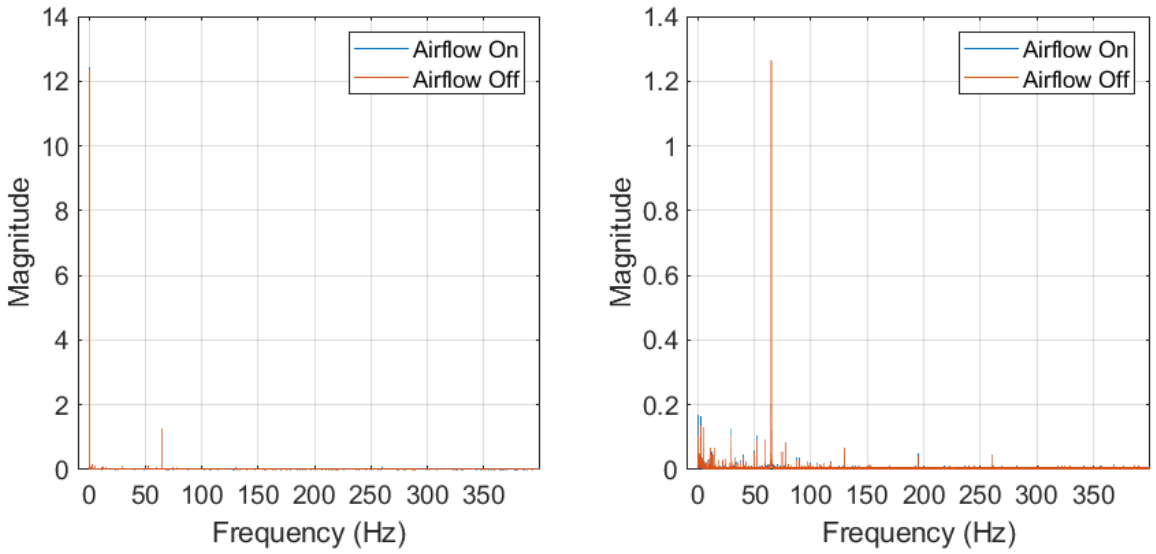

Figure 25. One-sided frequency spectrums of current measurements when VdG base and resistor were connected to a ground strip instead of the airfoil. Left: Raw data - The peaks for both airflow cases are at 0 Hz and approximately 65 Hz. Right: Raw data with mean subtracted - Peaks above 65 Hz are harmonics (130 Hz, 195 Hz, etc.).

The one-sided frequency spectrums of the raw data, both before and after subtracting out the its mean value, from the 2.54 cm spacing's first run with airflow off are shown in Figure 26 below. Like the grounded case, there were peaks at DC and approximately 65 Hz. This trend of DC and 65 Hz being the two most significant components continued across nearly all other runs, as can be seen in Tables 8 through

11 below. Some measurements did not feature 65 Hz in their top two values, although their plotted spectrums did contain peaks at that frequency. The persistence of the 65 Hz peaks throughout the with-airfoil runs lends further weight towards it being an artifact of the VdG. Based on the spectral data, future experiments with this VdG could decrease the SR560's cutoff frequency from 30 Hz and use a greater rolloff without losing meaningful information.

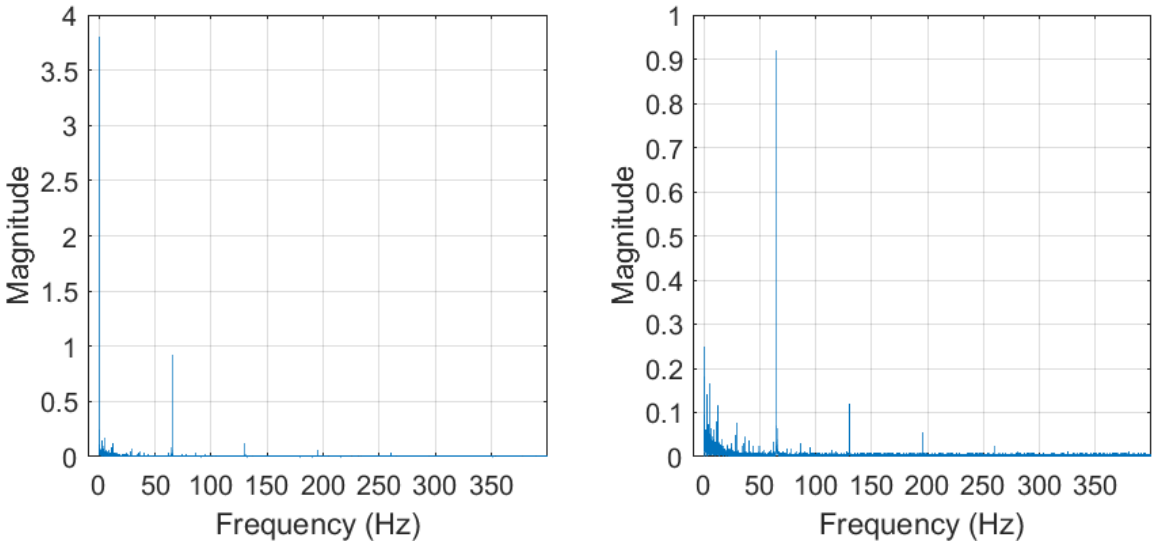

Figure 26. One-sided frequency spectrums of current measurements for 2.54 cm VdG-airfoil separation and no airflow. Left: Raw data - The peaks for both airflow cases are at 0 Hz and approximately 65 Hz. Right: Raw data with mean subtracted - Peaks above 65 Hz are harmonics (130 Hz, 195 Hz, etc.).

4.4 Adding Copper Wicks to Airfoil

The currents measured for each wick array are shown in Figure 27. The currents were again on the order of μA which corresponded to voltages on the order of mV. The sharp jump after 60 seconds in the 3 wicks plot was the jump mentioned previously in Section 4.3.1. That jump in current remained for many unrecorded trials but disappeared the following day. The process was repeated and the currents did not

Table 8. Two greatest magnitudes in one-sided frequency spectrums for the runs with airflow off (2.54 to 38.10 cm)

Spacing (cm)		2.54	7.62	15.24	22.86	30.48	38.10
Run 1 Peaks (Hz)	Peak 1	0	0	0	0	0	0
	Value	3.80	4.11	4.58	3.34	3.06	1.08
	Peak 2	65.10	65.06	5.60	65.13	65.10	65.03
	Value	0.92	0.32	0.28	1.27	0.67	0.31
Run 2 Peaks (Hz)	Peak 1	0	0	0	0	0	0
	Value	4.59	5.15	4.26	3.22	1.68	3.11
	Peak 2	65.06	0.07	65.16	65.16	65.10	65.03
	Value	0.69	0.30	0.28	0.83	1.29	0.57
Run 3 Peaks (Hz)	Peak 1	0	0	0	0	0	0
	Value	5.56	3.93	4.69	4.61	4	3.40
	Peak 2	65.06	0.03	65.16	64.86	65.10	65.06
	Value	0.58	0.29	1.08	1.27	0.80	0.29

Table 9. Two greatest magnitudes in one-sided frequency spectrums for the runs with airflow off (45.72 to 76.2 cm)

Spacing (cm)		45.72	53.34	60.96	68.58	76.20
Run 1 Peaks (Hz)	Peak 1	0	0	0	0	0
	Value	3.14	3.81	4.39	3.12	2.97
	Peak 2	65.03	65.16	65.16	65.16	65.10
	Value	0.95	0.59	0.67	0.86	0.26
Run 2 Peaks (Hz)	Peak 1	0	0	0	0	0
	Value	2.92	3.61	3.89	2.88	3.62
	Peak 2	65.06	65.20	65.16	65.13	0.03
	Value	0.62	0.56	0.58	0.64	0.35
Run 3 Peaks (Hz)	Peak 1	0	0	0	0	0
	Value	2.80	4.01	3.42	2.90	3.43
	Peak 2	65.06	65.16	65.13	65.13	5.57
	Value	0.61	0.80	0.64	1.28	0.27

Table 10. Two greatest magnitudes in one-sided frequency spectrums for the runs with airflow on (2.54 to 38.10 cm)

Spacing (cm)		2.54	7.62	15.24	22.86	30.48	38.10
Run 1 Peaks (Hz)	Peak 1	0	0	0	0	0	0
	Value	5.92	3.92	4.46	3.03	2.90	4.07
	Peak 2	65.06	0.03	2.80	65.16	65.06	65.03
	Value	0.76	0.39	0.28	1	0.64	0.78
Run 2 Peaks (Hz)	Peak 1	0	0	0	0	0	0
	Value	4.17	4.88	4.24	3.59	2.88	1.97
	Peak 2	65.06	0.03	65.20	65.20	65.10	65.10
	Value	0.74	0.72	0.33	0.79	0.66	1.05
Run 3 Peaks (Hz)	Peak 1	0	0	0	0	0	0
	Value	5.89	4.01	3.88	5.07	4.94	2.64
	Peak 2	65.10	5.50	65.16	64.83	65.10	65.10
	Value	0.92	0.25	0.43	1.42	0.61	0.95

Table 11. Two greatest magnitudes in one-sided frequency spectrums for the runs with airflow on (45.72 to 76.2 cm)

Spacing (cm)		45.72	53.34	60.96	68.58	76.20
Run 1 Peaks (Hz)	Peak 1	0	0	0	0	0
	Value	3	3.54	3.86	3.27	3.51
	Peak 2	65.06	65.16	65.16	65.16	0.03
	Value	0.86	0.58	1.15	0.68	0.51
Run 2 Peaks (Hz)	Peak 1	0	0	0	0	0
	Value	3.06	3.89	3.81	3.23	3.32
	Peak 2	65.10	65.16	65.16	65.20	5.57
	Value	0.98	0.49	0.92	0.80	0.29
Run 3 Peaks (Hz)	Peak 1	0	0	0	0	0
	Value	2.82	3.80	3.97	3.02	3.65
	Peak 2	65.10	65.16	65.16	65.16	65.13
	Value	0.66	0.72	0.64	0.61	1.66

exhibit any jumps until the 3 wick array, as is seen in Figure 28. However, the two jumps observed were short-lived and finished during the current run. There were no obvious visual or aural indicators for a current jump initiating or terminating.

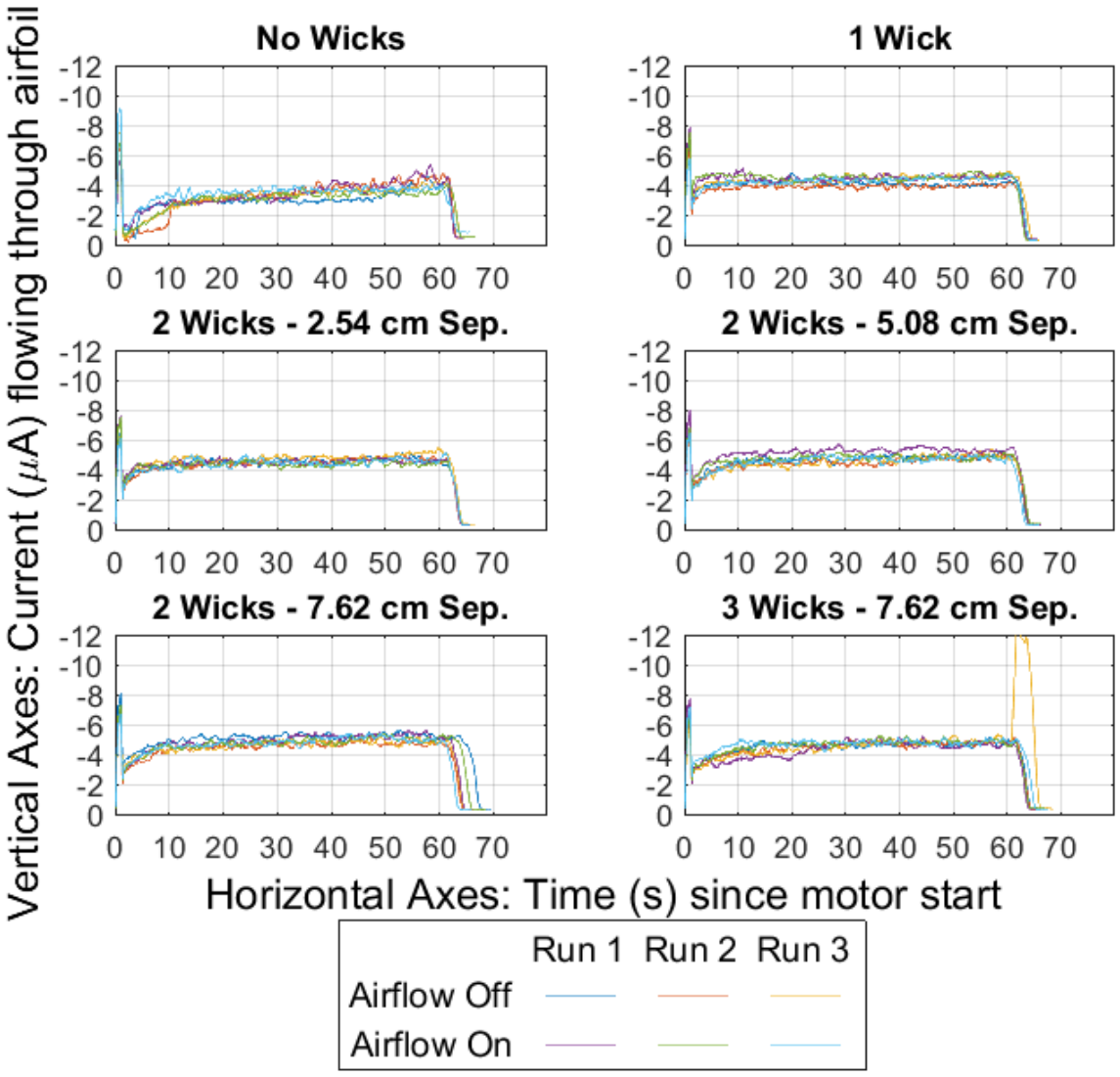

Figure 27. Current (μA) flowing through the aluminum airfoil as a function of time (s) since starting the VdG's motor. The VdG was 76.2 cm from the airfoil and each wick extended 7.62 cm toward the VdG.

The limiting currents for each wick array were calculated the same as was done in Section 4.3. Those currents are listed in Table 12 below. The $\hat{\mu}$ sample averages

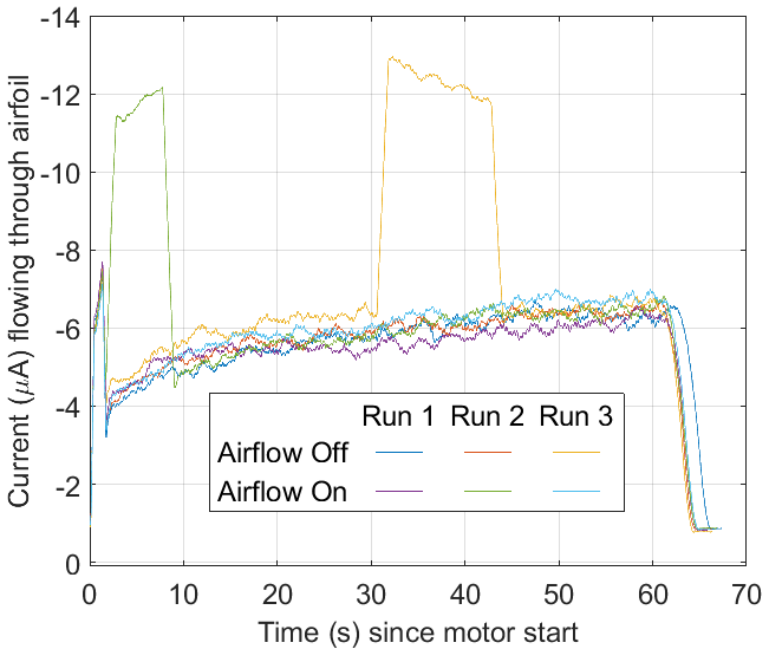

Figure 28. Repeating the current measurements for the three wick configuration on the aluminum airfoil showed that the unpredictable step jumps in current can be short-lived.

of the limiting currents are plotted below in Figure 29 with 95% confidence interval error bars. The upper and lower bounds for each interval are listed in Table 13. The confidence intervals for the individual airflow settings (on and off) used t-distributions with two degrees of freedom. The variance of the limiting currents of each arrangement are shown in Figure 30; they exhibit no obvious dependence upon the particular wick arrangement.

Based on the error bars in Figure 29, adding the passive copper wicks statistically improved the current output. The effect of the wicks was assessed using the airflow off case. The maximum current sample average was -4.88 μA at the 2 Wick - 7.62 cm separation, an approximately 46% increase from the -3.340 μA sample average in the no wick case. Higher sample averages were expected with more wicks, but the 3 Wick - 7.62 cm separation was expected to have the highest sample average. Based on the confidence interval bounds, that discrepancy is likely not meaningful.

Table 12. Limiting currents for each wick array attached to the aluminum airfoil. The values in each *Run* column were calculated by averaging the filtered current measurements from 20 to 50 seconds. The $\hat{\mu}$ columns are sample means of the limiting currents indicated by the subscript.

Wick Amt	Spacing (cm)	Limiting Current (μA)							
		Airflow Off				Airflow On			
		Run 1	Run 2	Run 3	$\hat{\mu}_{\text{off}}$	Run 1	Run 2	Run 3	$\hat{\mu}_{\text{on}}$
0	N/A	-2.973	-3.617	-3.431	-3.340	-3.509	-3.318	-3.651	-3.493
1	N/A	-4.092	-3.906	-4.438	-4.145	-4.447	-4.463	-4.376	-4.429
2	2.54	-4.609	-4.539	-4.747	-4.632	-4.501	-4.374	-4.467	-4.447
	5.08	-4.771	-4.544	-4.649	-4.655	-5.321	-4.884	-4.718	-4.974
	7.62	-5.201	-4.682	-4.782	-4.888	-5.086	-4.887	-4.941	-4.971
3	7.62	-4.637	-4.673	-4.646	-4.652	-4.665	-4.808	-4.782	-4.752

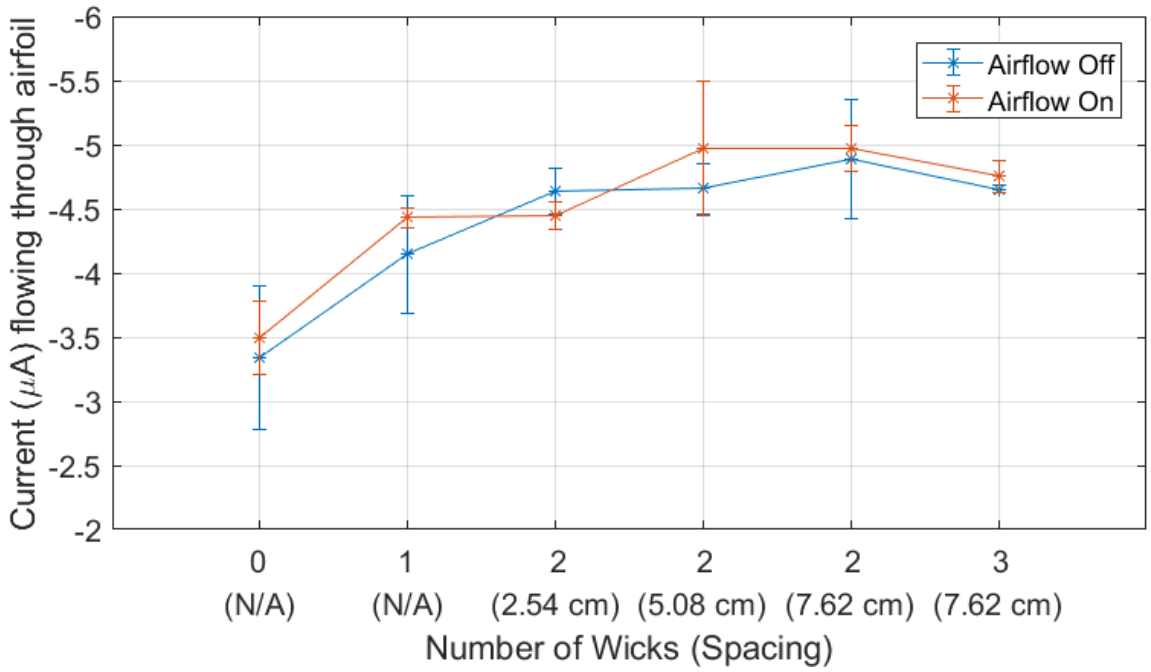

Figure 29. Sample averages of the aluminum airfoil limiting currents listed in Table 12 with 95% confidence interval error bars added. Confidence interval bounds are listed in Table 13

Table 13. Upper and lower bounds for the 95% confidence interval error bars displayed in Figure 29

Wick Amt	Spacing (cm)	95% Confidence Interval Bounds (μA)			
		Airflow Off		Airflow On	
		Upper	Lower	Upper	Lower
0	N/A	-4.163	-2.518	-3.907	-3.078
1	N/A	-4.816	-3.475	-4.544	-4.314
2	2.54	-4.895	-4.369	-4.611	-4.284
	5.08	-4.936	-4.373	-5.748	-4.201
	7.62	-5.573	-4.203	-5.227	-4.715
3	7.62	-4.699	-4.605	-4.942	-4.562

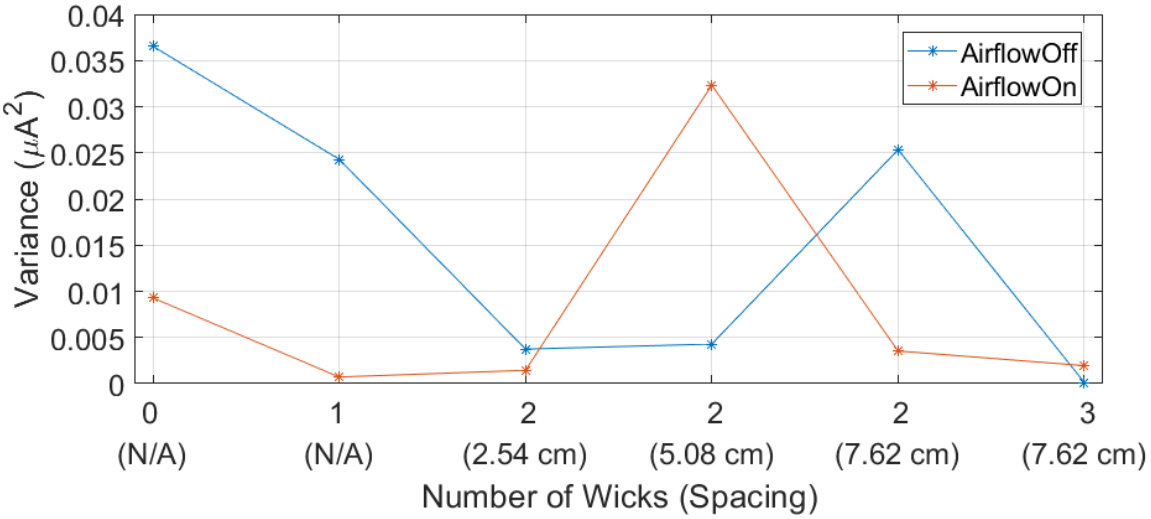

Figure 30. Current measurement variance for each wick arrangement on aluminum airfoil

The effect of airflow was assessed by subtracting the airflow off sample currents from the associated airflow on sample currents: $\mu_{\text{diff, i}} = \hat{\mu}_{\text{on, i}} - \hat{\mu}_{\text{off, i}}$. Then, a hypothesis test was constructed were the null hypothesis H_0 was that $\mu_{\text{diff}} = 0$ and the alternative hypothesis H_1 was that $\mu_{\text{diff}} < 0$ to see if having the airflow on caused a more negative current. The average difference was -0.1256 μA, the standard error was 0.0734 μA, there were five degrees of freedom, and the associated t-score was -1.7104. The residuals of each μ_{diff} are presented on a normal probability plot in Figure 31. There was deviation between the residuals and the probability plot, but not enough to prevent assuming an underlying gaussian distribution. The upper-tail residual at 0.31 μA corresponded to the 2 Wicks - 2.54 cm separation case and was retained because it was the only positive μ_{diff}. Based on these statistics, there was an approximately 7.39% chance that there was no statistically significant difference between the airflow settings and any observed differences were due to noise. Phrased differently, there was an approximately 92.61% chance that supplying airflow increased the current measurements.

Spectral analysis indicated similar trends to those discussed in Section 4.3.2 with DC and 65 Hz commonly being the two greatest magnitudes. The top two magnitudes in the one sided frequency spectra are listed in Tables 14 and 15 below.

4.5 Coating Airfoil with Electrically Insulating Paint

The aluminum airfoil was coated with a cermaic engine enamel that, based on multimeter readings, made the outer skin electrically insulative. The procedure of Section 4.4 was repeated. The current measurements are shown in Figure 32 below and the limiting currents are listed in Table 16. These currents are, at times, nearly double those seen in the prior experiment, but this comparison is not meaningful. The results shown in Figure 32 are from repeating the insulating airfoil experiment a

Table 14. Two greatest magnitudes in one-sided frequency spectrums for the runs with airflow off and wick arrays on aluminum airfoil

		Wick Number (Spacing [cm])					
		0 (N/A)	1 (N/A)	2 (2.54)	2 (5.08)	2 (7.62)	3 (7.62)
Run 1 Peaks (Hz)	Peak 1	0	0	0	0	0	0
	Value	2.974	4.095	4.609	4.771	5.202	4.635
	Peak 2	65.097	64.864	64.964	64.964	64.997	64.931
	Value	0.261	1.587	0.780	0.969	0.759	1.192
Run 2 Peaks (Hz)	Peak 1	0	0	0	0	0	0
	Value	3.619	3.905	4.538	4.547	4.683	4.670
	Peak 2	0.033	64.931	64.964	64.964	64.931	64.931
	Value	0.348	1.555	0.951	0.725	0.988	1.067
Run 3 Peaks (Hz)	Peak 1	0	0	0	0	0	0
	Value	3.432	4.438	4.747	4.651	4.783	4.646
	Peak 2	5.566	64.964	64.931	64.964	64.931	64.931
	Value	0.270	1.442	0.922	1.019	1.142	1.081

Table 15. Two greatest magnitudes in one-sided frequency spectrums for the runs with airflow on and wick arrays on aluminum airfoil

		Wick Number (Spacing [cm])					
		0 (N/A)	1 (N/A)	2 (2.54)	2 (5.08)	2 (7.62)	3 (7.62)
Run 1 Peaks (Hz)	Peak 1	0	0	0	0	0	0
	Value	3.507	4.445	4.503	5.320	5.084	4.665
	Peak 2	0.033	64.864	64.931	64.997	64.931	64.931
	Value	0.508	1.552	1.424	0.988	1.082	1.352
Run 2 Peaks (Hz)	Peak 1	0	0	0	0	0	0
	Value	3.316	4.464	4.375	4.885	4.886	4.808
	Peak 2	5.566	64.964	64.931	64.997	64.931	64.931
	Value	0.294	1.144	1.242	0.798	0.909	0.954
Run 3 Peaks (Hz)	Peak 1	0	0	0	0	0	0
	Value	3.653	4.377	4.467	4.716	4.939	4.781
	Peak 2	65.131	64.964	64.931	64.964	64.931	64.931
	Value	1.660	1.379	0.904	0.877	1.019	0.949

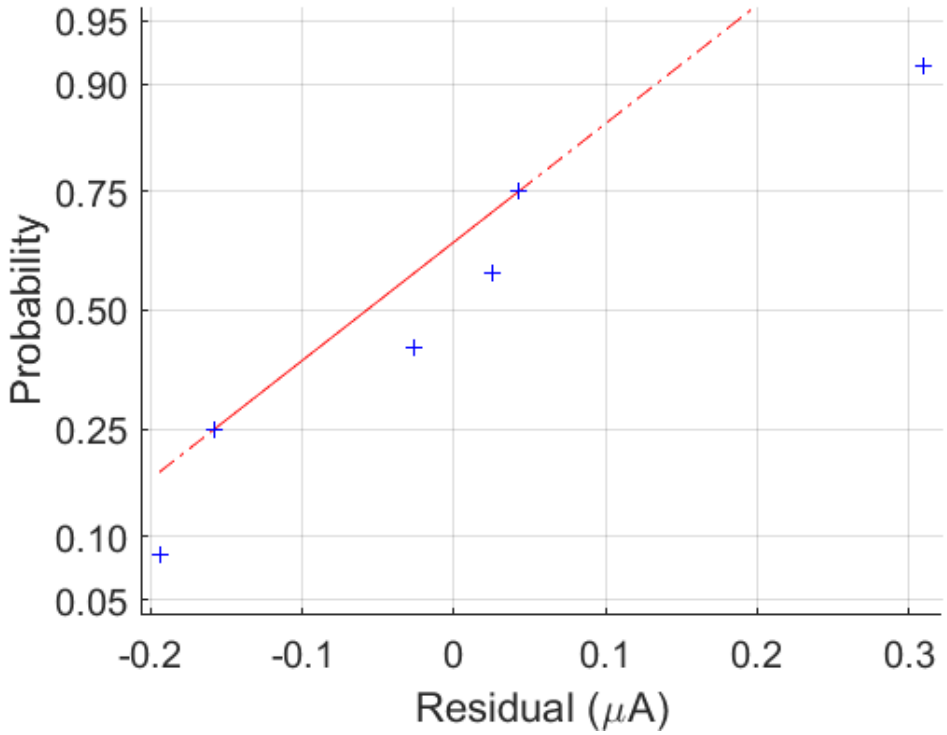

Figure 31. The aluminum airfoil μ_{diff} residuals deviated from a normal probability plot, but not enough to prevent assuming an underlying gaussian distribution. The upper-tail residual at 0.31 μA corresponded to the 2 Wicks - 2.54 cm separation case and was retained because it was the only positive μ_{diff}.

second time.

During the first attempt, a current jump occurred midway through and became persistent. Those measurements were not used due to a lack of intra-experiment consistency. The sample averages of the limiting currents listed in Table 16 are plotted in Figure 33 with 95% confidence interval error bars. The interval bounds are listed in Table 17. The variance of the limiting currents of each arrangement are shown in Figure 34. Based on the sample average plot, the airflow appeared to have no significant impact. Statistics supported this conclusion.

A hypothesis test was performed identically to the test in Section 4.4. There were still five degrees of freedom, but this time the average difference was 0.4638 μA, the

Table 16. Limiting currents for each wick array attached to the insulated airfoil. The values in each *Run* column were calculated by averaging the filtered current measurements from 20 to 50 seconds. The $\hat{\mu}$ columns are sample means of the limiting currents indicated by the subscript.

Wick Amt	Spacing (cm)	Limiting Current (μA)							
		Airflow Off				Airflow On			
		Run 1	Run 2	Run 3	$\hat{\mu}_{\text{off}}$	Run 1	Run 2	Run 3	$\hat{\mu}_{\text{on}}$
0	N/A	-10.824	-10.567	-5.834	-9.075	-7.970	-6.527	-5.836	-6.778
1	N/A	-10.593	-10.124	-10.527	-10.415	-10.657	-10.398	-10.081	-10.379
2	2.54	-10.902	-11.037	-10.599	-10.846	-10.421	-10.902	-10.878	-10.734
	5.08	-10.558	-11.246	-15.053	-12.285	-11.022	-11.069	-11.364	-11.152
	7.62	-12.103	-11.297	-11.693	-11.697	-12.307	-11.947	-11.419	-11.891
3	7.62	-13.718	-11.775	-12.082	-12.525	-13.578	-13.524	-12.284	-13.128

Table 17. Upper and lower bounds for the 95% confidence interval error bars displayed in Figure 33

Wick Amt	Spacing (cm)	95% Confidence Interval Bounds (μA)			
		Airflow Off		Airflow On	
		Upper	Lower	Upper	Lower
0	N/A	-16.055	-2.095	-9.482	-4.073
1	N/A	-11.046	-9.783	-11.096	-9.662
2	2.54	-11.404	-10.289	-11.406	-10.061
	5.08	-18.300	-6.271	-11.612	-10.692
	7.62	-12.699	-10.696	-13.001	-10.781
3	7.62	-15.119	-9.931	-14.946	-11.311

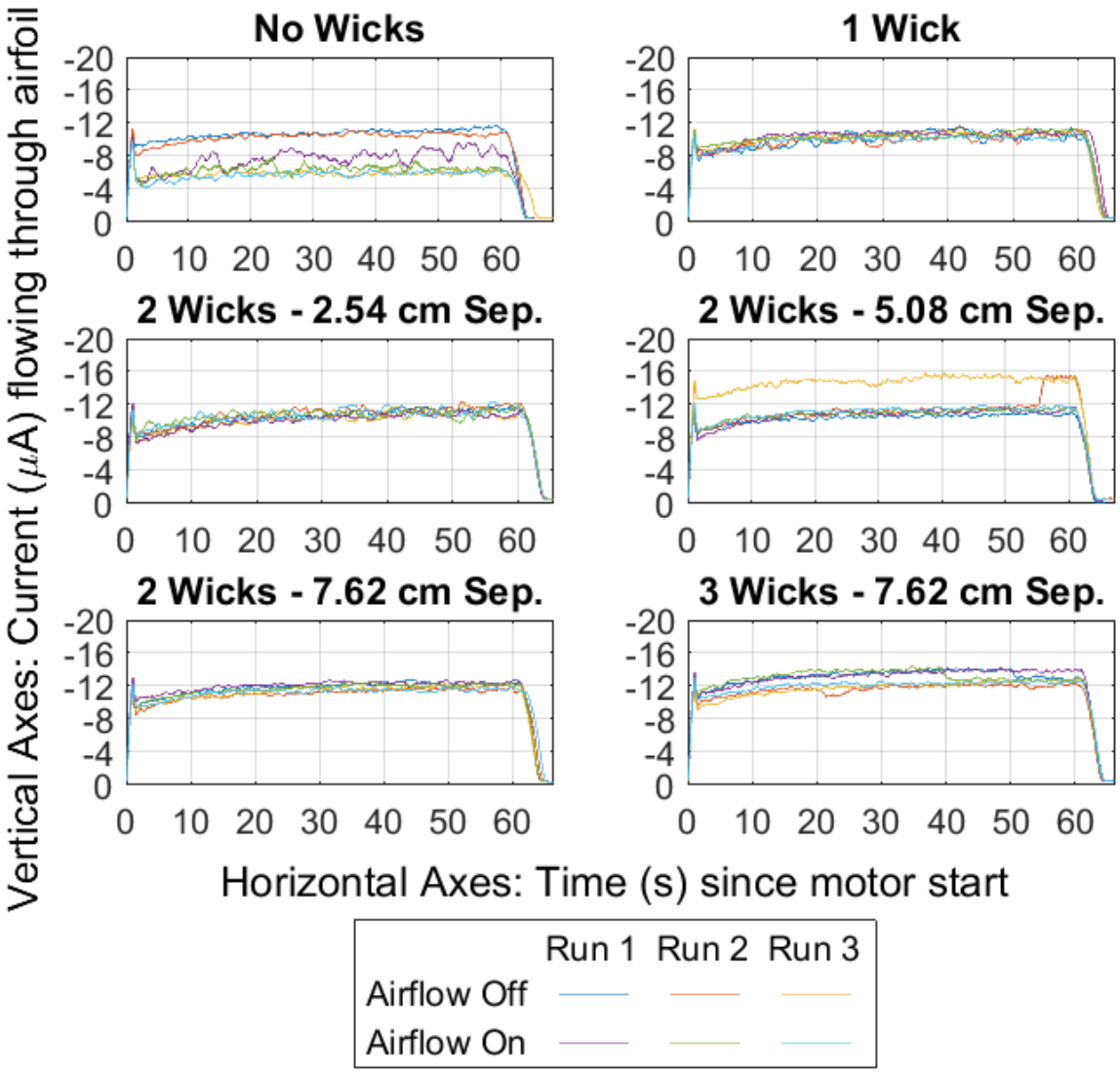

Figure 32. Current (μA) flowing through the insulated airfoil as a function of time (s) since starting the VdG's motor. The VdG was 76.2 cm from the airfoil and each wick extended 7.62 cm toward the VdG.

standard error was 0.4355 μA, and the associated t-score was 1.0651. The residuals of each μ_{diff} are presented on a normal probability plot in Figure 35 and do not show enough evidence to prevent assuming an underlying gaussian distribution. With these statistics, there was an approximately 83.22% chance that no statistically significant difference existed between the airflow settings. This result was not surprising

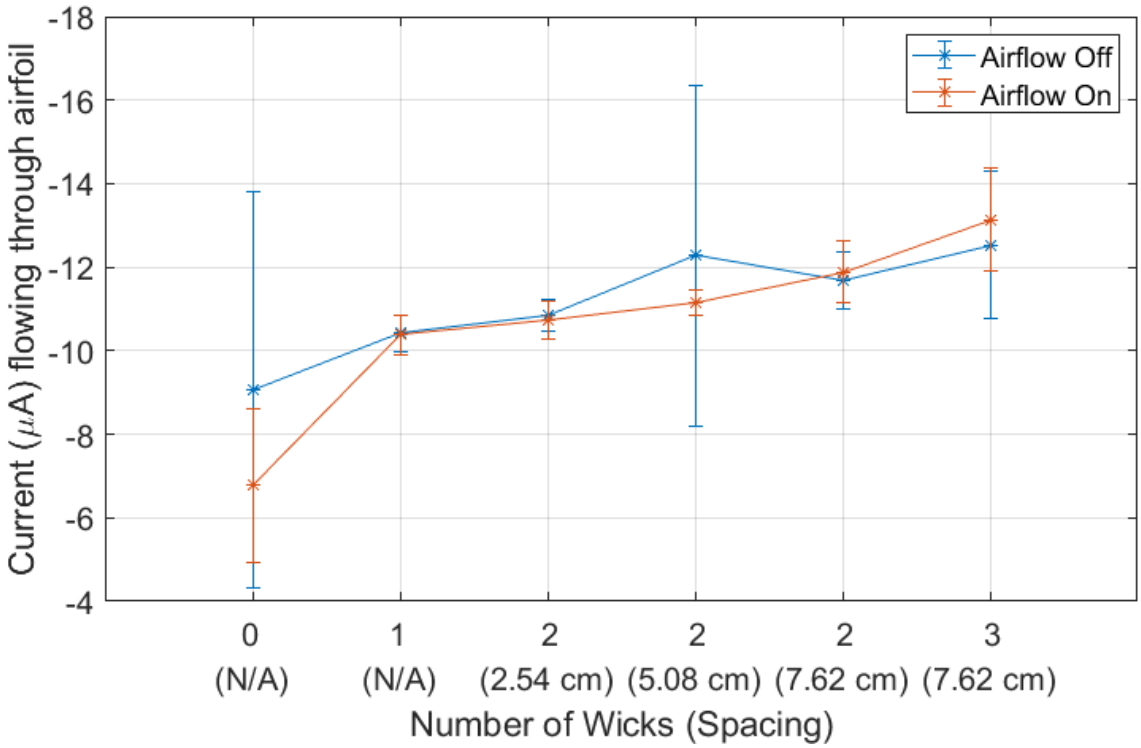

Figure 33. Sample averages of the insulating airfoil limiting currents listed in Table 16 with 95% confidence interval error bars added. Confidence interval bounds are listed in Table 17

because the airfoil's outer coating was now electrically insulative. This meant the electron's would have a lower mobility and faster airflow would be required to make a statistically significant impact on the current measurements.

A potential outlier existed within the 2 Wicks - 5.08 cm measurements. The third airflow off run in the associated subplot in Figure 32 was noticeably higher than the other five runs. A current jump occurred at the end of the second airflow off run, which was the run immediately prior, and persisted into the third airflow off run. In order to observe the third airflow off run's effect on the statistical conclusions, that run's limiting current, -15.053 μA was removed. Doing so dropped the associated airflow off sample average to -10.902 μA. The hypothesis test was repeated: the average difference was 0.2332 μA, the standard error was 0.4255 μA, and the associated t-

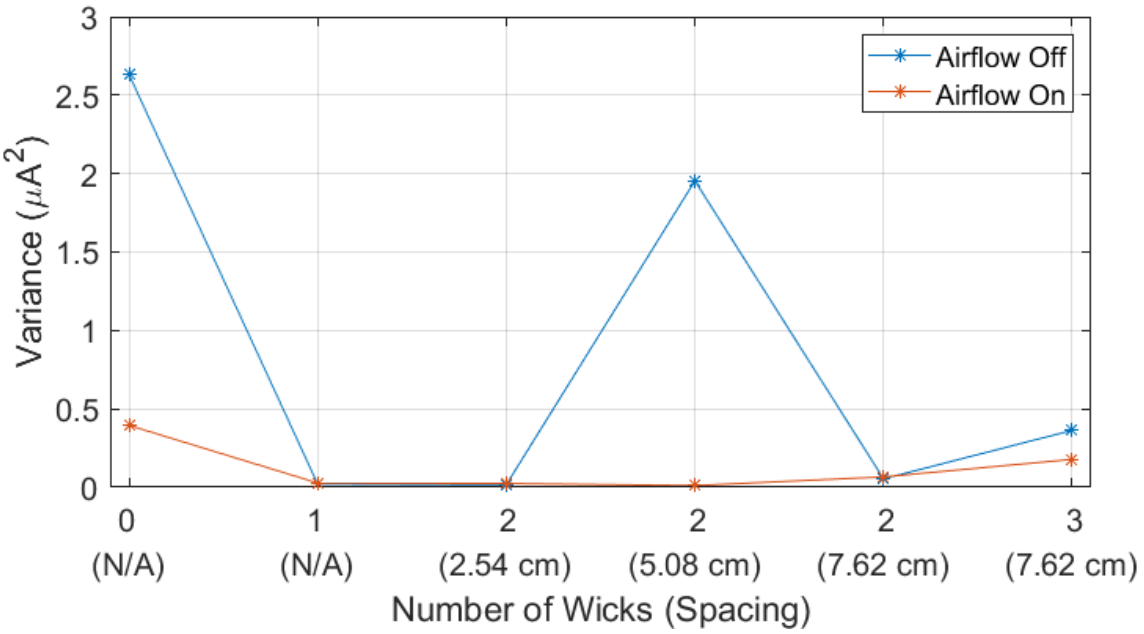

Figure 34. Current measurement variance for each wick arrangement on insulated airfoil

score was 0.5482. Now there was only an approximately 69.64% chance that no statistically significant difference existed between the airflow settings. Although the likelihood dropped 13.58%, the evidence still favored the previous test's conclusions.

The effect of adding wicks was assessed using the airflow off sample averages with the aforementioned potential outlier removed. The greatest sample average from the airflow off subset was -12.525 μA from the 3 Wicks - 7.62 cm separation configuration. This average was approximately 38% greater than the lowest sample average: -9.075 μA from the no wick case. With the insulating airfoil, unlike the conductive airfoil, the largest number of wicks produced the highest sample average.

Spectral analysis on this data set identified dominant DC and 65 Hz components just like the spacing experiment and the non-insulated airfoil experiment. The highest two magnitudes in each current measurement's one-side frequency spectrum are listed in Tables 18 and 19.

Table 18. Two greatest magnitudes in one-sided frequency spectrums for the runs with airflow off and wick arrays on insulated airfoil

		Wick Number (Spacing [cm])					
		0 (N/A)	1 (N/A)	2 (2.54)	2 (5.08)	2 (7.62)	3 (7.62)
Run 1 Peaks (Hz)	Peak 1	0	0	0	0	0	0
	Value	10.823	10.598	10.898	10.559	12.103	13.717
	Peak 2	64.997	64.931	64.931	64.964	64.931	64.931
	Value	1.292	1.666	1.733	1.076	1.3650	1.887
Run 2 Peaks (Hz)	Peak 1	0	0	0	0	0	0
	Value	10.567	10.124	11.040	11.247	11.296	11.776
	Peak 2	64.931	64.964	64.931	64.964	64.931	64.964
	Value	1.409	1.575	1.584	1.201	1.469	1.291
Run 3 Peaks (Hz)	Peak 1	0	0	0	0	0	0
	Value	5.835	10.525	10.603	15.048	11.695	12.081
	Peak 2	64.9310	64.964	64.931	64.931	64.931	64.964
	Value	1.289	1.428	1.582	1.499	1.347	1.531

Table 19. Two greatest magnitudes in one-sided frequency spectrums for the runs with airflow on and wick arrays on insulated airfoil

		Wick Number (Spacing [cm])					
		0 (N/A)	1 (N/A)	2 (2.54)	2 (5.08)	2 (7.62)	3 (7.62)
Run 1 Peaks (Hz)	Peak 1	0	0	0	0	0	0
	Value	7.966	10.661	10.423	11.021	12.308	13.577
	Peak 2	64.931	64.964	64.931	64.931	64.931	64.964
	Value	1.205	1.526	1.240	1.380	1.098	1.6780
Run 2 Peaks (Hz)	Peak 1	0	0	0	0	0	0
	Value	6.527	10.399	10.901	11.069	11.948	13.524
	Peak 2	64.964	64.931	64.931	64.931	64.931	64.964
	Value	1.537	1.147	1.643	1.267	1.267	1.4330
Run 3 Peaks (Hz)	Peak 1	0	0	0	0	0	0
	Value	5.838	10.081	10.874	11.363	11.421	12.283
	Peak 2	64.931	64.931	64.964	64.931	64.964	64.964
	Value	1.051	1.101	1.401	1.397	1.060	1.322

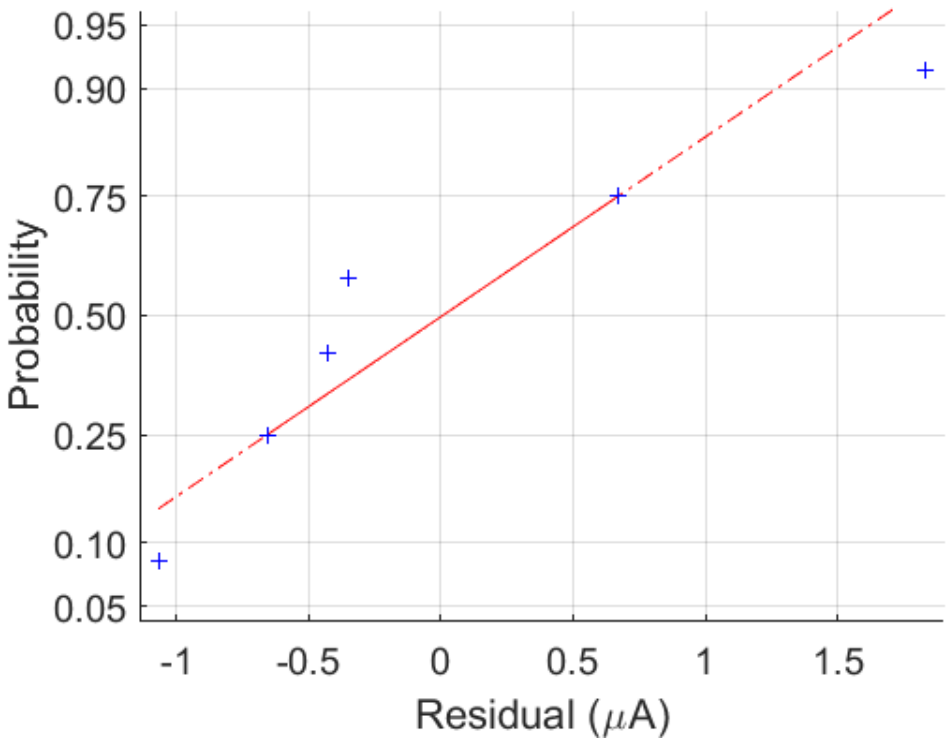

Figure 35. The insulating airfoil μ_{diff} residuals deviated from a normal probability plot, but not enough to prevent assuming an underlying gaussian distribution.

4.6 Summary

This section summarizes this chapter's findings. First, increasing the distance between the VdG and the airfoil reduced the current flowing out of the airfoil as well as the measurement variance. A separation distance of 76.2 cm was considered large enough to not be concerned with the VdG dome's electric field. Second, it can be said with 92.61% confidence that flowing air over the aluminum airfoil with various static wick arrays increased the current output. However, the current was on average only -0.1256 μA higher so the improvement was not extreme. The airfoil's tapered edge and conductive skin likely facilitated the charge removal. However, once the airfoil was coated with an electrically insulative ceramic paint, it was very unlikely that the

wind improved the current.

Statistical tests using all data for the insulated airfoil calculated a 83.22% chance that no statistically significant difference existed between the airflow settings. Removing a potential outlier dropped the likelihood to 69.64%. It was reasonable that no significant difference existed because the paint lowered the electrons' mobility which reduced the force exerted by the airflow onto the electrons. Overall, the ability of airflow to improve the performance of passive wicks appears dependent upon the charged body's surface conductivity. Finally, spectral analysis across all data sets indicated that, in addition to the expected DC component, a 65 Hz component typically had the second highest frequency spectrum magnitude. It was posited that, since the supply power was 60 Hz, the 65 Hz was the result of the supply power propagating through the machine.

V. Conclusion

5.1 Conclusions

This research sought to determine what impact airflow had on the current leaving an airfoil equipped with passive copper wicks. It can be concluded with 92.61% confidence that flowing air at 10 m/s over an aluminum airfoil did increase the current leaving an aluminum airfoil equipped with passive copper wicks. The average improvement, however, was only -0.1256 μA which was much smaller than the measured limiting currents. Those currents on average ranged from approximately -3.5 μA to -4.97 μA. It is posited that that airfoil's tapered edge and conductive surface create an environment already facilitating charge leaving the airfoil.

Conversely, flowing air at 10 m/s over an airfoil coated on the outside with ceramic, electrically insulating paint had no statistically significant effect. Although the airfoil's inner surface was still conductive and allowed for an even distribution of charge, the insulating outer surface damped the electrons' mobility. This meant air would need to be flown over the surface at a higher velocity in order to exert a statistically significant effect. The currents measured with the insulating airfoil were higher than the aluminum airfoil's currents, but that was a byproduct of a persistent jump in the Van de Graaff generator's output current. Consequently, comparisons of current measurements between experiments are not meaningful.

Based on the airflow off sample averages, adding passive wicks increased the average limiting current from the conductive airfoil by up to -1.548 μA, a 46% improvement. Similarly, the addition of passive wicks increased the average limiting current from the insulating airfoil by -3.450 μA which was an approximately 38% rise. This was expected based on wicks providing additional sharp edges for charge to leave the airfoil.

5.2 Future Research

There are many potential routes to take with this research. One way is to vary the airfoil's surface material or shape. A larger test cell could be used to provide space that can fit enough ducting to achieve laminar flow without an air filter present. Further, the airflow velocity test range could be expanded into the 30 to 50 m/s range. One could also create an environment representative of a particular altitude. Additionally, the required electricity could be provided via battery power instead of outlet power to control for fluctuations in the external power grid. Future work could also bias the wicks relative to the airfoil to create an active corona discharge system, or attach a high voltage power supply to the Van de Graaff generator's lower comb to increase the airfoil's charging current. After wicks and corona discharges are fully investigated, thermionic technology could be considered.

Bibliography

1. R. Tanner and J. Nanevicz, "Precipitation Charging and Corona-Generated Interference in Aircraft," Stanford Research Institute, Menlo Park, CA, Tech. Rep. AD0261029, Apr. 1961. [Online]. Available: https://apps.dtic.mil/sti/citations/AD0261029

2. B. Vonnegut and A. D. Little Inc., "Electrical Behavior of an Airplane in a Thunderstorm," Federal Aviation Agency, Cambridge, MA, Tech. Rep. AD0614914, Feb. 1965. [Online]. Available: https://apps.dtic.mil/sti/citations/AD0614914

3. R. Gunn, W. Hall, and G. Kinzer, "Army-Navy Precipitation-Static Project: Part I - The Precipitation-Static Interference Problem and Methods for Its Investigation," *Proceedings of the IRE*, vol. 34, no. 4, pp. 156–161, Apr. 1946. [Online]. Available: http://ieeexplore.ieee.org/document/1697045/

4. G. Kinzer and J. McGee, "Army-Navy Precipitation-Static Project: Part IV - Investigations of Methods for Reducing Precipitation-Static Radio Interference," *Proceedings of the IRE*, vol. 34, no. 5, pp. 234–240, May 1946. [Online]. Available: http://ieeexplore.ieee.org/document/1697059/

5. D. Pettit, A. Turnbull, and H. A. Roelant, "General Aviation Aircraft Reliability Study," NASA, Hampton, VA, Tech. Rep. CR-2001-210647, Feb. 2001. [Online]. Available: https://ntrs.nasa.gov/citations/20010027423

6. H. Hucke, "Precipitation-Static Interference on Aircraft and at Ground Stations," *Proceedings of the IRE*, vol. 27, no. 5, pp. 301–316, May 1939. [Online]. Available: http://ieeexplore.ieee.org/document/1686909/

7. R. Tanner, "Radio Interference from Corona Discharges," Stanford Research Institute, Stanford, CA, Tech. Rep. AD0012600, Apr. 1953. [Online]. Available: https://apps.dtic.mil/sti/citations/AD0012600

8. S. Chapman, "Discharge of Corona Point Current from Aircraft," Cornell Aeronautical Laboratory, Inc., Buffalo, NY, Tech. Rep. AD0118584, Dec. 1954. [Online]. Available: https://apps.dtic.mil/sti/citations/AD0118584

9. F. W. Peek, *Dielectric phenomena in high voltage engineering.* New York: New York: McGraw-Hill Book Company, Inc., 1924. [Online]. Available: https://archive.org/details/dielectricphenom00peekrich/page/40/mode/2up

10. C. F. Gallo, "Corona-A Brief Status Report," *IEEE Transactions on Industry Applications*, vol. IA-13, no. 6, pp. 550–557, Nov. 1977. [Online]. Available: http://ieeexplore.ieee.org/document/4503458/

11. J. J. Lowke and F. D'Alessandro, "Onset corona fields and electrical breakdown criteria," *Journal of Physics D: Applied Physics*, vol. 36, no. 21, pp. 2673–2682, Nov. 2003. [Online]. Available: https://iopscience.iop.org/article/10.1088/0022-3727/36/21/013

12. G. W. Trichel, "The Mechanism of the Negative Point to Plane Corona Near Onset," *Physical Review*, vol. 54, no. 12, pp. 1078–1084, Dec. 1938. [Online]. Available: https://link.aps.org/doi/10.1103/PhysRev.54.1078

13. W. L. Lama and C. F. Gallo, "Systematic study of the electrical characteristics of the "Trichel" current pulses from negative needle-to-plane coronas," *Journal of Applied Physics*, vol. 45, no. 1, pp. 103–113, Jan. 1974. [Online]. Available: http://aip.scitation.org/doi/10.1063/1.1662943

14. R. Morrow, "Theory of negative corona in oxygen," *Physical Review A*, vol. 32, no. 3, pp. 1799–1809, Sep. 1985. [Online]. Available: https://link.aps.org/doi/10.1103/PhysRevA.32.1799

15. Y. Zhang, Q. Xia, Z. Jiang, and J. Ouyang, "Trichel pulse in various gases and the key factor for its formation," *Scientific Reports*, vol. 7, no. 1, p. 10135, Dec. 2017. [Online]. Available: http://www.nature.com/articles/s41598-017-10118-2

16. T. Giao and J. Jordan, "Modes of Corona Discharges in Air," *IEEE Transactions on Power Apparatus and Systems*, vol. PAS-87, no. 5, pp. 1207–1215, May 1968. [Online]. Available: http://ieeexplore.ieee.org/document/4073624/

17. D. S. Antao, D. A. Staack, A. Fridman, and B. Farouk, "Atmospheric pressure dc corona discharges: operating regimes and potential applications," *Plasma Sources Science and Technology*, vol. 18, no. 3, p. 035016, Aug. 2009. [Online]. Available: https://iopscience.iop.org/article/10.1088/0963-0252/18/3/035016

18. Y. S. Akishev, M. E. Grushin, I. V. Kochetov, A. P. Napartovich, M. V. Pan'kin, and N. I. Trushkin, "Transition of a multipin negative corona in atmospheric air to a glow discharge," *Plasma Physics Reports*, vol. 26, no. 2, pp. 157–163, Feb. 2000. [Online]. Available: http://link.springer.com/10.1134/1.952826

19. Y. Akishev, M. Grushin, I. Kochetov, V. Karal'nik, A. Napartovich, and N. Trushkin, "Negative corona, glow and spark discharges in ambient air and transitions between them," *Plasma Sources Science and Technology*, vol. 14, no. 2, pp. S18–S25, May 2005. [Online]. Available: https://iopscience.iop.org/article/10.1088/0963-0252/14/2/S03

20. S. Chapman, "The Magnitude of Corona Point Discharge Current," *Journal of the Atmospheric Sciences*, vol. 34, no. 11, pp. 1801–1809, Nov. 1977. [Online]. Available: https://journals.ametsoc.org/view/journals/atsc/34/11/1520-0469_1977_034_1801_tmocpd_2_0_co_2.xml

21. S. Chapman, "Corona point current in wind," *Journal of Geophysical Research*, vol. 75, no. 12, pp. 2165–2169, Apr. 1970. [Online]. Available: http://doi.wiley.com/10.1029/JC075i012p02165

22. G. J. Born and E. J. Durbin, "An Investigation of Electrical Charging and Discharging of Aircraft in Flight," Princeton University, Princeton, NJ, Tech. Rep. AD0273976, Dec. 1961. [Online]. Available: https://apps.dtic.mil/sti/citations/AD0273976

23. J. de la Cierva and B. Poteate, "Helicopter Static Electricity Discharging Device," Kellett Aircraft Corporation, Willow Grove, PA, Tech. Rep. AD0406212, Dec. 1962. [Online]. Available: https://apps.dtic.mil/sti/citations/AD0406212

24. Dynasciences Corporation, "A High-Performance Electrostatic Discharger for Helicopters," Fort Washington PA: Dynasciences Corporation, Fort Washington PA, Tech. Rep., 1963. [Online]. Available: https://apps.dtic.mil/sti/citations/AD0600451

25. J. Nanevicz, "Alleviation Techniques for Effects of Static Charging on Avionics," in *AGARD Lecture Series No. 110*. London, UK: North Atlantic Treaty Organization, May 1980, pp. 203–216. [Online]. Available: https://apps.dtic.mil/sti/citations/ADA087976

26. C. Guerra-Garcia, N. C. Nguyen, J. Peraire, and M. Martinez-Sanchez, "Charge Control Strategy for Aircraft-Triggered Lightning Strike Risk Reduction," *AIAA Journal*, vol. 56, no. 5, pp. 1988–2002, May 2018. [Online]. Available: https://arc.aiaa.org/doi/10.2514/1.J056406

27. C. Guerra-Garcia, N. C. Nguyen, T. Mouratidis, and M. Martinez-Sanchez, "Corona Discharge in Wind for Electrically Isolated Electrodes," *Journal of Geophysical Research: Atmospheres*, vol. 125, no. 16, pp. 1–14, Aug. 2020. [Online]. Available: https://onlinelibrary.wiley.com/doi/10.1029/2020JD032908

28. C. Guerra-Garcia, P. Fontanes, M. Urbani, J. Montanya, T. Mouratidis, M. Martinez-Sanchez, and C. Nguyen, "Controlled Electric Charging of an Aircraft in Flight using Corona Discharge," in *AIAA Scitech 2020 Forum*, no. January. Reston Virginia: American Institute of Aeronautics and Astronautics, Jan. 2020, pp. 1–10. [Online]. Available: https://arc.aiaa.org/doi/10.2514/6.2020-1887

29. E. Moreau, "Airflow control by non-thermal plasma actuators," *Journal of Physics D: Applied Physics*, vol. 40, no. 3, pp. 605–636, Feb. 2007. [Online]. Available: https://iopscience.iop.org/article/10.1088/0022-3727/40/3/S01

30. A. Saveliev, V. Golub, V. Sechenov, and E. Son, "Dielectric Barrier Discharge Initiation Under the Supersonic Airflow," in *48th AIAA Aerospace Sciences*

Meeting Including the New Horizons Forum and Aerospace Exposition. Reston, Virigina: American Institute of Aeronautics and Astronautics, Jan. 2010, pp. 1–10. [Online]. Available: http://arc.aiaa.org/doi/10.2514/6.2010-467

31. D. V. Roupassov, A. A. Nikipelov, M. M. Nudnova, and A. Y. Starikovskii, "Flow Separation Control by Plasma Actuator with Nanosecond Pulsed-Periodic Discharge," *AIAA Journal*, vol. 47, no. 1, pp. 168–185, Jan. 2009. [Online]. Available: https://arc.aiaa.org/doi/10.2514/1.38113

32. M. Nishihara, K. Takashima, J. W. Rich, and I. V. Adamovich, "Mach 5 bow shock control by a nanosecond pulse surface dielectric barrier discharge," *Physics of Fluids*, vol. 23, no. 6, p. 066101, Jun. 2011. [Online]. Available: http://aip.scitation.org/doi/10.1063/1.3599697

33. J. Shang, S. Surzhikov, R. Kimmel, D. Gaitonde, J. Menart, and J. Hayes, "Mechanisms of plasma actuators for hypersonic flow control," *Progress in Aerospace Sciences*, vol. 41, no. 8, pp. 642–668, Nov. 2005. [Online]. Available: https://linkinghub.elsevier.com/retrieve/pii/S0376042105001235

34. V. I. Gibalov and G. J. Pietsch, "The development of dielectric barrier discharges in gas gaps and on surfaces," *Journal of Physics D: Applied Physics*, vol. 33, no. 20, pp. 2618–2636, Oct. 2000. [Online]. Available: https://iopscience.iop.org/article/10.1088/0022-3727/33/20/315

35. X. Xu, "Dielectric barrier discharge — properties and applications," *Thin Solid Films*, vol. 390, no. 1-2, pp. 237–242, Jun. 2001. [Online]. Available: https://linkinghub.elsevier.com/retrieve/pii/S0040609001009567

36. C. L. Enloe, T. E. McLaughlin, R. D. VanDyken, K. D. Kachner, E. J. Jumper, and T. C. Corke, "Mechanisms and Responses of a Single Dielectric Barrier Plasma Actuator: Plasma Morphology," *AIAA Journal*, vol. 42, no. 3, pp. 589–594, May 2004. [Online]. Available: https://arc.aiaa.org/doi/10.2514/1.2305

37. T. C. Corke, C. L. Enloe, and S. P. Wilkinson, "Dielectric barrier discharge plasma actuators for flow control," *Annual Review of Fluid Mechanics*, vol. 42, pp. 505–529, Jan. 2010. [Online]. Available: https://www.annualreviews.org/doi/abs/10.1146/annurev-fluid-121108-145550

38. J. J. Wang, K. S. Choi, L. H. Feng, T. N. Jukes, and R. D. Whalley, "Recent developments in DBD plasma flow control," *Progress in Aerospace Sciences*, vol. 62, pp. 52–78, Oct. 2013. [Online]. Available: https://www.sciencedirect.com/science/article/abs/pii/S0376042113000535

39. C. Louste, G. Artana, E. Moreau, and G. Touchard, "Sliding discharge in air at atmospheric pressure: electrical properties," *Journal of Electrostatics*, vol. 63, no. 6-10, pp. 615–620, Jun. 2005. [Online]. Available: https://linkinghub.elsevier.com/retrieve/pii/S0304388605000409

40. N. Zouzou, K. Takashima, E. Moreau, A. Mizuno, and G. Touchard, "Sliding discharge study in axisymmetric configuration," in *28th ICPIG*, Prague, Czech Republic, 2007, pp. 1007–1010. [Online]. Available: https://www.researchgate.net/profile/Noureddine_Zouzou/publication/268008118_Sliding_discharge_study_in_axisymmetric_configuration/links/54c0d4820cf28a6324a35106.pdf

41. B. Zheng, X. Ke, C. Ge, Y. Zhu, Y. Wu, F. Liu, and S. Luo, "Electrical and Flow Characteristics of a Double-Side Sliding Pulsed Discharge Plasma Actuator," *AIAA Journal*, vol. 58, no. 2, pp. 733–746, Feb. 2020. [Online]. Available: https://arc.aiaa.org/doi/10.2514/1.J058424

42. Q.-K. He, H. Liang, and B.-R. Zheng, "Discharge and flow characterizations of the double-side sliding discharge plasma actuator," *Chinese Physics B*, vol. 29, no. 6, p. 064702, Jun. 2020. [Online]. Available: https://iopscience.iop.org/article/10.1088/1674-1056/ab8624

43. R. Sosa, E. Arnaud, E. Memin, and G. Artana, "Study of the flow induced by a sliding discharge," *IEEE Transactions on Dielectrics and Electrical Insulation*, vol. 16, no. 2, pp. 305–311, Apr. 2009. [Online]. Available: http://ieeexplore.ieee.org/document/4815157/

44. H. Nishida, K. Nakai, and T. Matsuno, "Physical mechanism of tri-electrode plasma actuator with direct-current high voltage," *AIAA Journal*, vol. 55, no. 6, pp. 1852–1861, Mar. 2017. [Online]. Available: https://arc.aiaa.org/doi/10.2514/1.J055560

45. H. Xu, N. Gomez-Vega, D. R. Agrawal, and S. R. H. Barrett, "Higher thrust-to-power with large electrode gap spacing electroaerodynamic devices for aircraft propulsion," *Journal of Physics D: Applied Physics*, vol. 53, no. 2, p. 025202, Jan. 2020. [Online]. Available: https://iopscience.iop.org/article/10.1088/1361-6463/ab4a4c

46. C. K. Gilmore and S. R. Barrett, "Electroaerodynamic Thruster Performance as a Function of Altitude and Flight Speed," *AIAA Journal*, vol. 56, no. 3, pp. 1105–1117, Mar. 2018. [Online]. Available: https://arc.aiaa.org/doi/10.2514/1.J056138

47. N. Monrolin, F. Plouraboué, and O. Praud, "Electrohydrodynamic Thrust for In-Atmosphere Propulsion," *AIAA Journal*, vol. 55, no. 12, pp. 4296–4305, Dec. 2017. [Online]. Available: https://arc.aiaa.org/doi/10.2514/1.J055928

48. E. Moreau, P. Audier, and N. Benard, "Ionic wind produced by positive and negative corona discharges in air," *Journal of Electrostatics*, vol. 93, pp. 85–96, Jun. 2018. [Online]. Available: https://doi.org/10.1016/j.elstat.2018.03.009

49. A. Kahn, "Fermi level, work function and vacuum level," *Materials Horizons*, vol. 3, no. 1, pp. 7–10, Oct. 2016. [Online]. Available: http://xlink.rsc.org/?DOI=C5MH00160A

50. R. d. L. Kronig and W. Penney, "Quantum mechanics of electrons in crystal lattices," *Proceedings of the Royal Society of London. Series A, Containing Papers of a Mathematical and Physical Character*, vol. 130, no. 814, pp. 499–513, Feb. 1931. [Online]. Available: https://royalsocietypublishing.org/doi/10.1098/rspa.1931.0019

51. F. Bloch, "Über die Quantenmechanik der Elektronen in Kristallgittern," *Zeitschrift für Physik*, vol. 52, no. 7-8, pp. 555–600, Jul. 1929. [Online]. Available: http://link.springer.com/10.1007/BF01339455

52. K. L. Jensen, "A tutorial on electron sources," *IEEE Transactions on Plasma Science*, vol. 46, no. 6, pp. 1881–1899, Jun. 2018. [Online]. Available: https://ieeexplore.ieee.org/document/8252746/

53. K. Jensen, *Introduction to the Physics of Electron Emission*. Chichester, UK: John Wiley & Sons, Ltd, Nov. 2017. [Online]. Available: http://doi.wiley.com/10.1002/9781119051794

54. S. Dushman, "Electron Emission from Metals as a Function of Temperature," *Physical Review*, vol. 21, no. 6, pp. 623–636, Jun. 1923. [Online]. Available: https://link.aps.org/doi/10.1103/PhysRev.21.623

55. C. Crowell, "Richardson constant and tunneling effective mass for thermionic and thermionic-field emission in Schottky barrier diodes," *Solid-State Electronics*, vol. 12, no. 1, pp. 55–59, Jan. 1969. [Online]. Available: https://linkinghub.elsevier.com/retrieve/pii/003811016990135X

56. C. Herring and M. H. Nichols, "Thermionic Emission," *Reviews of Modern Physics*, vol. 21, no. 2, pp. 185–270, Apr. 1949. [Online]. Available: https://link.aps.org/doi/10.1103/RevModPhys.21.185

57. A. Kiejna, "On the temperature dependence of the work function," *Surface Science Letters*, vol. 178, no. 1-3, p. A652, Dec. 1986. [Online]. Available: https://linkinghub.elsevier.com/retrieve/pii/0167258486901593

58. L. W. Swanson, M. A. Gesley, and P. R. Davis, "Crystallographic dependence of the work function and volatility of LaB6," *Surface Science*, vol. 107, no. 1, pp. 263–289, May 1981. [Online]. Available: https://www.sciencedirect.com/science/article/abs/pii/0039602881906257

59. L. Uribarri and E. H. Allen, "Electron Transpiration Cooling for Hot Aerospace Surfaces," in *20th AIAA International Space Planes and Hypersonic Systems and Technologies Conference*. Glasgow, Scotland: American Institute of

Aeronautics and Astronautics, Jul. 2015. [Online]. Available: http://arc.aiaa.org/doi/10.2514/6.2015-3674

60. K. M. Hanquist and I. D. Boyd, "Limits for Thermionic Emission from Leading Edges of Hypersonic Vehicles," in *54th AIAA Aerospace Sciences Meeting*. San Diego, California: American Institute of Aeronautics and Astronautics, Jan. 2016. [Online]. Available: http://arc.aiaa.org/doi/10.2514/6.2016-0507

61. K. M. Hanquist, H. Alkandry, and I. D. Boyd, "Evaluation of Computational Modeling of Electron Transpiration Cooling at High Enthalpies," *Journal of Thermophysics and Heat Transfer*, vol. 31, no. 2, pp. 283–293, Apr. 2017. [Online]. Available: https://arc.aiaa.org/doi/10.2514/1.T4932

62. K. M. Hanquist and I. D. Boyd, "Effectiveness of Thermionic Emission for Cooling Hypersonic Vehicle Surfaces," in *2018 AIAA Aerospace Sciences Meeting*. Kissimmee, Florida: American Institute of Aeronautics and Astronautics, Jan. 2018. [Online]. Available: https://arc.aiaa.org/doi/10.2514/6.2018-1714

63. K. M. Hanquist and I. D. Boyd, "Plasma Assisted Cooling of Hot Surfaces on Hypersonic Vehicles," *Frontiers in Physics*, vol. 7, pp. 1–13, Feb. 2019. [Online]. Available: https://www.frontiersin.org/article/10.3389/fphy.2019.00009/full

64. D. M. Goebel and I. Katz, "Introduction," in *Fundamentals of Electric Propulasion*. Hoboken, NJ: John Wiley & Sons, Inc., Jul. 2008, ch. 1, pp. 1–13. [Online]. Available: http://doi.wiley.com/10.1002/9780470436448.ch1

65. D. M. Goebel and I. Katz, *Fundamentals of Electric Propulasion: Ion and Hall Thrusters*. Hoboken, NJ: John Wiley & Sons, Inc., Oct. 2008. [Online]. Available: http://doi.wiley.com/10.1002/9780470436448

66. D. M. Goebel and I. Katz, "Hollow Cathodes," in *Fundamentals of Electric Propulasion*. Hoboken, NJ: John Wiley & Sons, Inc., Jul. 2008, ch. 6, pp. 243–323. [Online]. Available: http://doi.wiley.com/10.1002/9780470436448.ch6

67. G. Becatti, D. M. Goebel, J. E. Polk, and P. Guerrero, "Life Evaluation of a Lanthanum Hexaboride Hollow Cathode for High-Power Hall Thruster," *Journal of Propulsion and Power*, vol. 34, no. 4, pp. 893–900, Jul. 2018. [Online]. Available: https://arc.aiaa.org/doi/10.2514/1.B36659

68. G. Becatti, D. M. Goebel, C. V. Yoke, A. L. Ortega, and I. G. Mikellides, "High Current Hollow Cathode for the X3 100-kW Class Nested Hall Thruster," in *36th International Electric Propulsion Conference*, Vienna, Austria, 2019. [Online]. Available: http://electricrocket.org/2019/371.pdf

69. L. Garrigues, "Computational Study of Hall-Effect Thruster with Ambient Atmospheric Gas as Propellant," *Journal of Propulsion and Power*, vol. 28,

no. 2, pp. 344–354, Mar. 2012. [Online]. Available: https://arc.aiaa.org/doi/10.2514/1.B34307

70. L. Pekker and M. Keidar, "Analysis of Airbreathing Hall-Effect Thrusters," *Journal of Propulsion and Power*, vol. 28, no. 6, pp. 1399–1405, Nov. 2012. [Online]. Available: https://arc.aiaa.org/doi/10.2514/1.B34441

71. K. H. Schoenbach, R. Verhappen, T. Tessnow, F. E. Peterkin, and W. W. Byszewski, "Microhollow cathode discharges," *Applied Physics Letters*, vol. 68, no. 1, pp. 13–15, Jan. 1996. [Online]. Available: http://aip.scitation.org/doi/10.1063/1.116739

72. B. Du, S. Mohr, D. Luggenhölscher, and U. Czarnetzki, "An atmospheric pressure self-pulsing micro thin-cathode discharge," *Journal of Physics D: Applied Physics*, vol. 44, no. 12, p. 125204, Mar. 2011. [Online]. Available: https://iopscience.iop.org/article/10.1088/0022-3727/44/12/125204

73. T. Asaka, T. Inagaki, T. Magome, N. Nishimori, Y. Otake, T. Taniuchi, K. Yanagida, and H. Tanaka, "Low-emittance radio-frequency electron gun using a gridded thermionic cathode," *Physical Review Accelerators and Beams*, vol. 23, no. 6, p. 063401, Jun. 2020. [Online]. Available: https://link.aps.org/doi/10.1103/PhysRevAccelBeams.23.063401

74. T. Yokoyama, T. Kobayashi, H. Murata, E. Rokuta, H. Shiroyama, H. Yasuda, and Y. Ooae, "Development of a Low-Work-Function Thermionic Cathode by Coating with LaB6 and Carbide," in *2018 31st International Vacuum Nanoelectronics Conference (IVNC)*. Kyoto, Japan: IEEE, Jul. 2018, pp. 1–2. [Online]. Available: https://ieeexplore.ieee.org/document/8520073/

75. M. Bakr, M. Kawai, T. Kii, and H. Ohgaki, "CeB6 : Emission Performance and Uniformity Compared With LaB6 for Thermionic RF Guns," *IEEE Transactions on Electron Devices*, vol. 63, no. 3, pp. 1326–1332, Mar. 2016. [Online]. Available: http://ieeexplore.ieee.org/document/7399711/

76. P. Cochems, M. Runge, and S. Zimmermann, "A current controlled miniaturized non-radioactive electron emitter for atmospheric pressure chemical ionization based on thermionic emission," *Sensors and Actuators A: Physical*, vol. 206, pp. 165–170, Feb. 2014. [Online]. Available: http://dx.doi.org/10.1016/j.sna.2013.11.033

77. J. M. D. Kowalczyk, M. R. Hadmack, E. B. Szarmes, and J. M. J. Madey, "Emissivity of Lanthanum Hexaboride Thermionic Electron Gun Cathode," *International Journal of Thermophysics*, vol. 35, no. 8, pp. 1538–1544, Aug. 2014. [Online]. Available: http://link.springer.com/10.1007/s10765-014-1712-3

78. J. Zhao, D. Gamzina, N. Li, J. Li, A. G. Spear, L. Barnett, M. Banducci, S. Risbud, and N. C. Luhmann, "Scandate Dispenser Cathode Fabrication for A

High-Aspect-Ratio High-Current-Density Sheet Beam Electron Gun," *IEEE Transactions on Electron Devices*, vol. 59, no. 6, pp. 1792–1798, Jun. 2012. [Online]. Available: http://ieeexplore.ieee.org/document/6178794/

79. M. E. Herniter and W. D. Getty, "Thermionic Cathode Electron Gun for High Current Densities," *IEEE Transactions on Plasma Science*, vol. 15, no. 4, pp. 351–360, Aug. 1987. [Online]. Available: http://ieeexplore.ieee.org/document/4316719/

80. X. Yuan, Y. Zhang, M. T. Cole, Y. Yan, X. Li, R. Parmee, J. Wu, N. Xu, W. I. Milne, and S. Deng, "A truncated-cone carbon nanotube cold-cathode electron gun," *Carbon*, vol. 120, pp. 374–379, Aug. 2017. [Online]. Available: http://dx.doi.org/10.1016/j.carbon.2017.03.046

81. N. Kumar, D. K. Pal, R. P. Lamba, U. N. Pal, and R. Prakash, "Analysis of Geometrical Design Parameters for High-Energy and High-Current-Density Pseudospark-Sourced Electron Beam Emission," *IEEE Transactions on Electron Devices*, vol. 64, no. 6, pp. 2688–2693, Jun. 2017. [Online]. Available: http://ieeexplore.ieee.org/document/7917277/

82. A. P. L. Guimarães, D. Carinhana, and A. Oliveira, "Characterization of an Electron Gun Based on a Pseudospark for Application in Hypersonic Shock Tunnels," in *45th AIAA Plasmadynamics and Lasers Conference*. Reston, Virginia: American Institute of Aeronautics and Astronautics, Jun. 2014, pp. 1–7. [Online]. Available: http://arc.aiaa.org/doi/10.2514/6.2014-2539

83. W. R. Huang, A. Fallahi, X. Wu, H. Cankaya, A.-L. Calendron, K. Ravi, D. Zhang, E. A. Nanni, K.-H. Hong, and F. X. Kärtner, "Terahertz-driven, all-optical electron gun," *Optica*, vol. 3, no. 11, p. 1209, Nov. 2016. [Online]. Available: https://www.osapublishing.org/abstract.cfm?URI=optica-3-11-1209

84. R. Nagai, R. Hajima, N. Nishimori, T. Muto, M. Yamamoto, Y. Honda, T. Miyajima, H. Iijima, M. Kuriki, M. Kuwahara, S. Okumi, and T. Nakanishi, "High-voltage testing of a 500-kV dc photocathode electron gun," *Review of Scientific Instruments*, vol. 81, no. 3, p. 033304, Mar. 2010. [Online]. Available: http://aip.scitation.org/doi/10.1063/1.3354980

85. N. Manivannan, W. Balachandran, C. Ribton, R. Beleca, M. Abbod, M. Cox, and P. Anastasia, "Chromium coated silicon nitride electron beam exit window," *Vacuum*, vol. 113, pp. 19–23, Mar. 2015. [Online]. Available: http://dx.doi.org/10.1016/j.vacuum.2014.11.024

86. M. Sámel, M. Stano, M. Zahoran, M. Ries, and Š. Matejčík, "Experimental characterisation of atmospheric pressure electron gun," *International Journal of Mass Spectrometry*, vol. 439, pp. 34–41, May 2019. [Online]. Available: https://linkinghub.elsevier.com/retrieve/pii/S1387380618303920

87. J. Lowell, "Contact electrification of metals," *Journal of Physics D: Applied Physics*, vol. 8, no. 1, pp. 53–63, Jan. 1975. [Online]. Available: https://iopscience.iop.org/article/10.1088/0022-3727/8/1/013

88. W. R. Harper, "The Volta effect as a cause of static electrification," *Proceedings of the Royal Society of London. Series A. Mathematical and Physical Sciences*, vol. 205, no. 1080, pp. 83–103, Jan. 1951. [Online]. Available: https://royalsocietypublishing.org/doi/10.1098/rspa.1951.0019

89. J. Lowell, "Surface states and the contact electrification of polymers," *Journal of Physics D: Applied Physics*, vol. 10, no. 1, pp. 65–71, Jan. 1977. [Online]. Available: https://iopscience.iop.org/article/10.1088/0022-3727/10/1/008

90. Shaw, P. E., "Experiments on tribo-electricity. I.—The tribo-electric series," *Proceedings of the Royal Society of London. Series A, Containing Papers of a Mathematical and Physical Character*, vol. 94, no. 656, pp. 16–33, Nov. 1917. [Online]. Available: https://royalsocietypublishing.org/doi/10.1098/rspa.1917.0046

91. H. A. Mizes, E. M. Conwell, and D. P. Salamida, "Direct observation of ion transfer in contact charging between a metal and a polymer," *Applied Physics Letters*, vol. 56, no. 16, pp. 1597–1599, Apr. 1990. [Online]. Available: http://aip.scitation.org/doi/10.1063/1.103139

92. H. Xu, Y. He, K. L. Strobel, C. K. Gilmore, S. P. Kelley, C. C. Hennick, T. Sebastian, M. R. Woolston, D. J. Perreault, and S. R. H. Barrett, "Flight of an aeroplane with solid-state propulsion," *Nature*, vol. 563, no. 7732, pp. 532–535, Nov. 2018. [Online]. Available: http://www.nature.com/articles/s41586-018-0707-9

93. H. Zou, Y. Zhang, L. Guo, P. Wang, X. He, G. Dai, H. Zheng, C. Chen, A. C. Wang, C. Xu, and Z. L. Wang, "Quantifying the triboelectric series," *Nature Communications*, vol. 10, no. 1, p. 1427, Dec. 2019. [Online]. Available: http://www.nature.com/articles/s41467-019-09461-x

94. R. J. Van de Graaff, K. T. Compton, and L. C. Van Atta, "The Electrostatic Generation of High Voltages for Nuclear Investigations," *The British Journal of Radiology*, vol. 6, no. 64, pp. 217–217, Apr. 1933. [Online]. Available: http://www.birpublications.org/doi/10.1259/0007-1285-6-64-217-b

95. J. Smee, "A 700-kV direct-current electrostatic generator," *Journal of the Institution of Electrical Engineers - Part I: General*, vol. 91, no. 47, pp. 422–431, Nov. 1944. [Online]. Available: https://ieeexplore.ieee.org/document/5294147

96. R. J. Kress, "Analysis of a Van De Graaff Generator for EMP Direct Current Survivability Testing," M.S. thesis, Dept. Eng. Phys., AFIT (AU),

Wright-Patterson AFB, OH, 2013. [Online]. Available: https://scholar.afit.edu/etd/935/

97. J. S. Leahy, "Experimental Testing of a Van De Graaff Generator as an Electromagnetic Pulse Generator," M.S. thesis, Dept. Eng. Phys., AFIT (AU), Wright-Patterson AFB, OH, 2016. [Online]. Available: https://apps.dtic.mil/sti/citations/AD1017975

98. Stanford Research Systems, *Model SR560 Low-Noise Preamplifier* (2013). [Online]. Available: https://www.thinksrs.com/downloads/pdfs/manuals/SR560m.pdf

99. Keysight Technologies, *InfiniiVision 3000T X-Series Oscilloscopes* (2020). [Online]. Available: https://www.keysight.com/us/en/assets/7018-04570/data-sheets/5992-0140.pdf

REPORT DOCUMENTATION PAGE

Form Approved
OMB No. 0704–0188

1. REPORT DATE *(DD–MM–YYYY)*	2. REPORT TYPE	3. DATES COVERED *(From — To)*
25–03–2021	Master's Thesis	Sept 2019 — Mar 2021

4. TITLE AND SUBTITLE

Charge Mitigation Technologies for Aircraft Platforms

5a. CONTRACT NUMBER

5b. GRANT NUMBER

5c. PROGRAM ELEMENT NUMBER

6. AUTHOR(S)

Rudy, Mitchell L., 1st Lt, USAF

5d. PROJECT NUMBER

5e. TASK NUMBER

5f. WORK UNIT NUMBER

7. PERFORMING ORGANIZATION NAME(S) AND ADDRESS(ES)

Air Force Institute of Technology
Graduate School of Engineering and Management (AFIT/EN)
2950 Hobson Way
WPAFB OH 45433-7765

8. PERFORMING ORGANIZATION REPORT NUMBER

AFIT-ENG-MS-21-M-078

9. SPONSORING / MONITORING AGENCY NAME(S) AND ADDRESS(ES)

Air Force Research Lab
Mark Fernelius, PhD
Bldg 490, 1790 Loop Rd N.
WPAFB OH 45433-7103
COMM 937-713-0047
Email: mark.fernelius.2@us.af.mil

10. SPONSOR/MONITOR'S ACRONYM(S)

AFRL

11. SPONSOR/MONITOR'S REPORT NUMBER(S)

12. DISTRIBUTION / AVAILABILITY STATEMENT

DISTRIBUTION STATEMENT A:
APPROVED FOR PUBLIC RELEASE; DISTRIBUTION UNLIMITED.

13. SUPPLEMENTARY NOTES

14. ABSTRACT

Research into ion-based advanced propulsion systems, such as air-breathing Hall effect thrusters on high-velocity aircraft and ion-propelled thrusters on spacecraft, necessitates addressing accompanying residual electric charge accumulation on the ungrounded flight platform. An experimental testbed was constructed to assess charge mitigation technologies and their effectiveness on aircraft. A Van de Graaff generator provided static charge accumulation levels exceeding a megavolt when combined with a high voltage direct current source generator. This research attached an isolated airfoil structure to the Van de Graaff generator's lower terminal to measure the induced leakage current under various applied environmental conditions, including up to three static wicks along the structure's trailing edge, airflow across the structure of up to 10 m/s, and an insulative painted coating. The airfoil was a symmetric teardrop shape; air flowed over the rounded edge first to the tapered edge. Statistical tests indicated airflow improved a conductive airfoil's leakage current at $\alpha = 0.0739$. The average increase was -0.1256 μA. No statistically significant improvements were observed with an insulative airfoil.

15. SUBJECT TERMS

Electrostatics, Aircraft, Charging, Corona Discharge

16. SECURITY CLASSIFICATION OF:			17. LIMITATION OF ABSTRACT	18. NUMBER OF PAGES	19a. NAME OF RESPONSIBLE PERSON
a. REPORT	b. ABSTRACT	c. THIS PAGE			Andrew S. Keys, Ph.D, AFIT/ENY
U	U	U	UU	104	19b. TELEPHONE NUMBER *(include area code)* (937) 255-3636, x4747; andrew.keys@afit.edu